

# **Assessment of wall-modeled large-eddy simulation for high-speed flows and novel modeling strategies**

By

Emily Jane Williams

B.S. Aerospace Engineering

University of Illinois Urbana-Champaign, 2021

Submitted to the Department of Aeronautics and Astronautics  
in Partial Fulfillment of the Requirements for the Degree of

MASTER OF SCIENCE IN AERONAUTICS AND ASTRONAUTICS

at the

MASSACHUSETTS INSTITUTE OF TECHNOLOGY

May 2023

© 2023 Emily Jane Williams. All rights reserved.

The author hereby grants to MIT a nonexclusive, worldwide,  
irrevocable, royalty-free license to exercise any and all rights under  
copyright, including to reproduce, preserve, distribute and publicly  
display copies of the thesis, or release the thesis under an open-access  
license.

Authored by: Emily Jane Williams  
Department of Aeronautics and Astronautics  
May 23, 2023

Certified by: Adrián Lozano-Durán  
Draper Assistant Professor of Aeronautics and Astronautics  
Thesis Supervisor

Accepted by: Jonathan P. How  
R. C. Maclaurin Professor of Aeronautics and Astronautics  
Chair, Graduate Program Committee



**Assessment of wall-modeled large-eddy simulation for  
high-speed flows and novel modeling strategies**

by

Emily Jane Williams

Submitted to the Department of Aeronautics and Astronautics  
on May 23, 2023, in Partial Fulfillment of the  
Requirements for the Degree of  
Master of Science in Aeronautics and Astronautics

**Abstract**

Turbulent flows are ubiquitous in aerospace engineering. External aerodynamic applications have exposed limitations in current state-of-the-art computational fluid dynamics solvers due to the presence of chaotic and multiscale turbulent flows. Wall-modeled large-eddy simulation (WMLES) stands as a realistic contender for turbulence modeling for aerospace applications. However, there remain important challenges of WMLES in the accurate prediction of certain quantities of interest within the stringest tolerance demanded by the industry. In this work, we evaluate the performance of WMLES for high-speed flows and explore new modeling venues. We assess the performance of WMLES for canonical compressible channel flows and a realistic external aerodynamic application, the Lockheed Martin X-59 Quiet Super-Sonic Technology (QueSST) aircraft. Additionally, we propose potential modeling improvements to enhance the predictive capabilities of WMLES for high-speed flows.

Thesis Supervisor: Adrián Lozano-Durán  
Title: Draper Assistant Professor of Aeronautics and Astronautics



## Acknowledgments

I want to thank many friends, family, and mentors - near and far, old and new - for unwavering compassion and understanding throughout my time at MIT so far. This work would not have been possible without the incredible support I have received from those invested in my happiness and well-being as a person and my success as a researcher and learner, and I am extremely grateful. I want to acknowledge my research advisor Adrian for introducing me to turbulence, always pushing me to do my best work, and prioritizing the best interests of my career.

I am very thankful to the Department of Energy Computational Science Graduate Fellowship and the Krell Institute for not only supporting my research endeavors, but also for giving me the freedom and ability to find a place in academia where I can thrive. I also want to thank the MIT Supercloud team and the Lincoln Laboratory Supercomputing Center for providing high-performance computing resources and consultation that have contributed to this work.



## Funding

This material is based upon work supported by the U.S. Department of Energy, Office of Science, Office of Advanced Scientific Computing Research, Department of Energy Computational Science Graduate Fellowship under Award Number DE-SC0023112. This report was prepared as an account of work sponsored by an agency of the United States Government. Neither the United States Government nor any agency thereof, nor any of their employees, makes any warranty, express or implied, or assumes any legal liability or responsibility for the accuracy, completeness, or usefulness of any information, apparatus, product, or process disclosed, or represents that its use would not infringe privately owned rights. Reference herein to any specific commercial product, process, or service by trade name, trademark, manufacturer, or otherwise does not necessarily constitute or imply its endorsement, recommendation, or favoring by the United States Government or any agency thereof. The views and opinions of authors expressed herein do not necessarily state or reflect those of the United States Government or any agency thereof.



# Contents

<b>1</b>	<b>Introduction</b>	<b>15</b>
1.1	Computational fluid dynamics for aerospace applications . . . . .	15
1.2	Fundamentals of turbulent flows . . . . .	17
1.3	Computational cost of simulating turbulence . . . . .	22
1.4	Compressibility effects in high-speed turbulence . . . . .	23
1.5	Objectives and outline . . . . .	26
<b>2</b>	<b>Technical approach and methodology</b>	<b>29</b>
2.1	Large-eddy simulation for compressible flows . . . . .	29
2.1.1	Conservation equations for compressible flow . . . . .	29
2.1.2	Filtering operator . . . . .	32
2.1.3	Governing equations of large-eddy simulation . . . . .	35
2.2	Existing subgrid-scale models . . . . .	36
2.2.1	Dynamic Smagorinsky model . . . . .	36
2.2.2	Vreman model . . . . .	37
2.3	Novel information-preserving model . . . . .	38
2.3.1	Preliminary concepts of information theory . . . . .	38
2.3.2	Information theory for modeling . . . . .	40
2.3.3	Information-preserving model . . . . .	42
2.4	Wall-modeled large-eddy simulation . . . . .	43
2.5	Numerical solver . . . . .	45
2.6	Supercomputing resources . . . . .	45

<b>3 Canonical case: compressible turbulent channel flow</b>	<b>47</b>
3.1 Objectives . . . . .	47
3.2 Physical and computational setup . . . . .	48
3.3 Quantities of interest . . . . .	49
3.4 Theoretical estimations . . . . .	49
3.5 Numerical results . . . . .	52
3.5.1 Dynamic Smagorinsky model . . . . .	52
3.5.2 Information-preserving model . . . . .	65
3.6 Conclusions . . . . .	66
<b>4 External aerodynamic application: X-59 QueSST</b>	<b>67</b>
4.1 Objectives . . . . .	67
4.2 Physical and computational setup . . . . .	69
4.3 Numerical results . . . . .	75
4.3.1 Shock waves . . . . .	75
4.3.2 Pressure signatures . . . . .	81
4.3.3 Error convergence . . . . .	82
4.4 Computational cost . . . . .	85
4.5 Conclusions . . . . .	87
<b>5 Conclusions</b>	<b>89</b>
5.1 Summary . . . . .	89
5.2 Outlook . . . . .	90
<b>A Non-dimensional compressible conservation equations</b>	<b>95</b>

# List of Figures

1-1	Canonical channel flow. . . . .	20
1-2	Visualization of eddies of turbulent channel flow. . . . .	21
2-1	Wall model for channel flow. . . . .	43
3-1	Canonical channel flow. . . . .	48
3-2	Mean temperature profiles. . . . .	53
3-3	Error scaling of mean temperature profile. . . . .	54
3-4	Percent error of mean temperature profile for all flow cases. . . . .	55
3-5	Mean velocity profiles. . . . .	56
3-6	Error scaling of mean velocity profile. . . . .	57
3-7	Percent error of mean velocity profile for all flow cases. . . . .	58
3-8	Heat flux at the wall with Mach number. . . . .	59
3-9	Error scaling of heat flux at the wall with Mach number. . . . .	60
3-10	Percent error of heat flux at the wall for all flow cases. . . . .	61
3-11	Skin friction coefficient with Mach number. . . . .	62
3-12	Error scaling of mean velocity profile. . . . .	63
3-13	Percent error of skin friction coefficient for all flow cases. . . . .	64
3-14	Mean profile predictions from IP and DSM SGS models. . . . .	65
4-1	Sonic boom prediction process [40]. . . . .	68
4-2	C608 configuration [40]. . . . .	70
4-3	C608 boundary conditions. . . . .	70
4-4	Computational domain for X-59 simulations. . . . .	72

4-5	Aircraft surface geometry and refinement in Gmsh. . . . .	73
4-6	Domain discretization views. . . . .	74
4-7	Pressure contour visualization from $x$ - $z$ plane. . . . .	77
4-8	Pressure contour visualization from $x$ - $y$ plane. . . . .	78
4-9	Pressure distribution from $x$ - $z$ plane. . . . .	79
4-10	Pressure distribution from $x$ - $y$ plane. . . . .	80
4-11	Near-field pressure signatures using DSM SGS model for different grid resolutions (cases 1-3). . . . .	81
4-12	Near-field pressure signatures using Vreman and DSM SGS models (cases 3 and 6). . . . .	82
4-13	Schematic of aircraft with delineations at specified locations. . . . .	83
4-14	Pressure convergence for different grid resolutions. . . . .	83
4-15	Error convergence for near-field pressure signature prediction. . . . .	84
4-16	Computational cost for number of control volumes in millions. . . . .	87

# List of Tables

2.1	MGHPCC TX-E1 specifications	46
3.1	Channel flow cases for WMLES	49
3.2	Error scaling properties for mean temperature profile	55
3.3	Error scaling properties for mean velocity profile	58
3.4	Error scaling properties for heat flux at the wall	60
3.5	Error scaling properties for skin friction coefficient	63
3.6	Error scaling properties for quantities of interest	65
3.7	Percent error in mean velocity and temperature profiles	66
4.1	X-59 QuSST error estimates	68
4.2	C608 freestream and boundary conditions	71
4.3	X-59 flow cases for WMLES	75
4.4	$L_2$ norms for near-field pressure signature predictions	85
4.5	Computational cost estimates for WMLES with Vreman SGS model	86



# Chapter 1

## Introduction

### 1.1 Computational fluid dynamics for aerospace applications

Computational fluid dynamics (CFD) has been instrumental in modeling and simulating flows in a variety of engineering problems, acting as a key tool for modern aircraft design. The use of CFD for external aerodynamic applications with increasing functionality and performance has greatly improved our understanding and predictive capabilities of complex flows [53]. However, these applications often entail the presence of turbulent flows, which have since exposed limitations in even the most advanced CFD solvers due to their multiscale nature in both time and space. Understanding the complex phenomena that emerge in turbulence involves careful consideration of the intersection of physics and mathematics. One outstanding challenge in CFD is the design of high-speed vehicles at high Mach numbers, as turbulent boundary layers determine the aerodynamic drag and heat transfer.

Direct numerical simulation (DNS) consists of resolving all scales of motion when solving the flow field [37]. It is often too computationally expensive to resolve all scales of motion involved in simulating turbulent flows at high Reynolds numbers and high Mach numbers. For aerospace applications in industry, Reynolds-averaged Navier-Stokes (RANS) modeling is most widely used. RANS-based turbulence modeling is

the standard approach to predict a wide range of flows for complex aerospace vehicles. RANS solvers are desired due to usability and computational efficiency. Additionally, these models are generally able to capture wall-bounded flows that we see in aerospace applications, as well as flows with shear, streamline curvature and rotation, and mild separation [53, 23]. Recently, large-eddy simulation (LES) has gained momentum as a framework for modeling the broad range of flow regimes of interest across industry and academia. Examples include separated flows, shock waves, and laminar-to-turbulent transition, to name a few. At high Reynolds numbers, LES is complemented by a wall model which accounts for the smallest energy eddies in the vicinity of the wall. This approach is referred to as wall-modeled LES (WMLES). The cost-efficiency of WMLES and its demonstrated predictive capabilities make it a realistic contender for turbulence modeling [2]. However, there remain important challenges of LES for external aerodynamic applications, such as the accurate prediction of aerodynamic coefficients and other quantities of interest within the stringest tolerance demanded by the industry. The current subgrid-scale (SGS) models are too simplistic to yield reliable predictions of statistical quantities of interest for complex geometries, such as supersonic aircraft, while maintaining an affordable computational cost.

Improving the tradeoff between accuracy and computational cost of WMLES using novel modeling techniques will lead to significant financial benefits across industries. From a medical perspective, turbulence is found in biofluids and blood vessels. Ocean currents, atmospheric cycles, pollution, and other gases also experience turbulence. Understanding the effects of turbulence can also help to improve infrastructure and transportation, such as bridge supports over rivers.

For the aerospace industry, these enhanced models would allow for a leap toward technology readiness for aircraft certification via CFD for aerospace vehicles across the range of high-speed flows from transonic to hypersonic, accelerating the development of advanced aircraft design via cost-effective virtual testing, reducing the design cost while maintaining safety and reliability [53]. The cost savings of these efforts are estimated in tens of billions while also lowering fuel consumption in the transportation sector. For perspective, ocean shipping consumes nearly 2 billion barrels of oil

per year, airline industries consume 1.5 billion, and trucking industries consume 1.2 billion [36]. The impact on the reduction of emissions of CO<sub>2</sub> and pollutants enabled by enhanced models will be equally impressive. Thus, the models will be directly applicable to improving WMLES for all regimes of high-speed flows, from hypersonic flight with re-entry vehicles to sustainable aviation for transonic and supersonic flight.

## 1.2 Fundamentals of turbulent flows

Turbulent flows are ubiquitous in engineering. In a turbulent flow, the velocity field is random. It follows that there seems to be an inherent inconsistency between the random nature of turbulent flows and the deterministic nature of the Navier-Stokes equations. However, we actually can have deterministic equations of motion with random solutions. In a turbulent flow, there are perturbations in both initial conditions and boundary conditions, as well as in material properties. Further, turbulent flow fields demonstrate very acute sensitivities to these perturbations. While such perturbations are also observed in laminar flows, turbulent flows occurring at high Reynolds numbers and high Mach numbers are more sensitive to small perturbations that grow with the evolution of the flow field. This behavior is well-known for chaotic dynamical systems, such as the Lorenz equations [30]. Extreme sensitivity to initial conditions results in the system reaching a certain point where the state cannot be predicted. Thus, for a complex set of deterministic equations, such as the Navier-Stokes equations, acute sensitivity to initial conditions is observed, and this directly contributes to the unpredictability of the solution.

It has been shown that turbulent motions range in size, from the width of the flow (normally assigned  $\delta$ ) to the smaller scales. The smallest turbulent motions become increasingly smaller when compared to  $\delta$  as the Reynolds number increases [48]. At high Reynolds number, there is a separation of scales. Mixing is controlled by the large-scale motions, which are most heavily influenced by the geometry and boundary conditions. Small-scale motions are governed by the viscosity of the flow and the rate at which the smaller scales receive energy from the larger scales.

This idea of the energy cascade, first proposed by Richardson in 1922 [49], is that kinetic energy is introduced in the turbulence through production at the largest scales. To better understand the cascade of energy, it is helpful to view each turbulent motion as an “eddy”. Turbulence can be composed of eddies of different sizes. Each eddy has some size  $l$ , characteristic velocity  $u(l)$ , and timescale  $\tau(l) \equiv l/u(l)$ . The sizes of the eddies in the flow are mostly coherent across the different regions. The largest eddies are characterized by the lengthscale  $l_0$  which is of the order of the flow scale  $\mathcal{L}$ . Further, the largest eddies have a characteristic velocity that is comparable to  $\mathcal{U}$ . Thus, it can be deduced that the Reynolds number of these largest eddies  $\text{Re}_0$  is large since it is comparable to  $\text{Re}$ , which we assume to be large. Therefore, we know the effects of viscosity are negligible. The largest eddies are unstable and transfer their energy to the relatively smaller-scale eddies as they are broken up, and this process continues. The energy is cascaded to the smallest scales by inviscid processes, at which point it is then dissipated by viscous processes. In other words, the energy cascade continues until the Reynolds number is small enough such that the motion of the eddies is stable and therefore the viscosity effectively dissipates the kinetic energy. Because dissipation signals the end of the process, it is found that the rate of dissipation is determined by the initial transfer of energy from the largest eddies. This conclusion is supported by experimental studies of free shear flows in that the energy cascade also demonstrates that this rate of dissipation is independent of viscosity at high Reynolds numbers [47].

Kolmogorov expanded on this idea of an energy cascade in theorizing that the velocity  $u(l)$  and timescale  $\tau(l)$  of the eddies decrease as  $l$  decreases [25]. Kolmogorov’s hypothesis of local isotropy says that at sufficiently high Reynolds number, the small-scale turbulent motions are statistically isotropic. Kolmogorov’s first similarity hypothesis further asserted that the statistics of these small-scale motions have a universal form that is uniquely determined by the viscosity and rate of dissipation. This theory resulted in a representation of the very smallest eddies in terms of the rate of

dissipation  $\varepsilon$  and the viscosity  $\nu$  defined by

$$\eta \equiv (\nu^3/\varepsilon)^{1/4}, \quad (1.1)$$

$$u_\eta \equiv (\varepsilon\nu)^{1/4}, \quad (1.2)$$

$$\tau_\eta \equiv (\nu/\varepsilon)^{1/2}, \quad (1.3)$$

which are now called the Kolmogorov length, velocity, and time scales [25]. It can be deduced that the Reynolds number based on the Kolmogorov scales is unity, which is consistent with Richardson's earlier work. The dissipation rate given by  $\varepsilon = \nu/\tau_\eta^2$  also is consistent in characterizing the velocity gradients of the smallest, dissipative eddies. Further, on the small scales, the velocity fields are statistically similar, still under the assumption of high Reynolds number turbulent flows. In other words, the velocity fields are statistically identical when scaled by the Kolmogorov scales, due to self-similarity.

Lastly, Kolmogorov's second similarity hypothesis combines this with insight from the ratios of the lengthscales at smaller and larger scales to say that the statistics of the motions of scales sufficiently in between  $l_0$  and  $\eta$  in what is called the inertial subrange are still dependent by the rate of dissipation  $\varepsilon$ , but independent of  $\nu$ . It is found that  $u(l)$  and  $\tau(l)$  decrease at  $l$  decreases within this inertial subrange. Further, the rate at which energy is transferred from larger eddies to smaller eddies is independent of  $l$  and equal to  $\varepsilon$  within the inertial subrange [25]. Viscous effects are negligible in the inertial subrange where motions are determined by inertial effects. Contrastingly, motions in the dissipation range naturally experience very strong viscous effects and thus account for effectively all of the dissipation that ends up halting the energy cascade process, in line with Richardson. Lastly, the largest eddies contain the most energy and are therefore found in the energy-containing range.

Many engineering applications include wall-bounded turbulence, which introduces additional complexities for high-speed flows. Wall flows can include internal flows, such as the flow through a channel, or external flows, such as the flow around an aircraft. We consider a fully developed channel flow that is statistically stationary

and statistically one-dimensional, with statistics depending only on the wall-normal direction. The flow is characterized by the Reynolds number. In contrast to free shear flows, the viscous stress dominates at the wall, and the wall shear stress is often a quantity of interest [43]. The channel flow can be broken up into different regions based on wall units ( $y^+$ ), starting with the viscous wall region close to the wall. In the outer layer, furthest from the wall, the direct effect of viscosity is negligible. The region essentially overlapping the inner and outer layers is the log-law region, a region of self-similarity for the mean velocity parallel to the wall at high Reynolds numbers. Figure 1-1 shows a schematic for channel flow, where  $\langle u \rangle$  is the mean velocity along the  $x$ -direction. The channel domain is defined by the channel half-height  $\delta = 1$ .

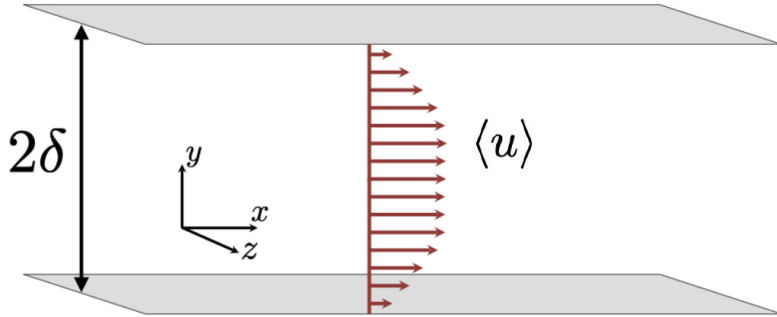


Figure 1-1: Canonical channel flow.

The attached eddy model is based on the hypothesis proposed by Townsend (1976) [57] that considers wall turbulence as a field of randomly distributed eddies with an important property: the velocity fields of the main eddies, regarded as persistent, organized flow patterns, extend to the wall and, in a sense, they are attached to the wall. In other words, Townsend's attached eddy hypothesis is a statement about the scaling of the dominant coherent motions in the logarithmic region. The hypothesis is only that velocity fields of those eddies scale with distance from the wall. The attached eddy hypothesis describes a property of the main eddies - inertial motions unaffected by viscosity. The statement also implies that the inertial scales (energy-containing motions) that dominate the logarithmic region are large relative to the viscous lengthscale. Therefore, Townsend's statement is that such motions must feel the presence of a wall that they are close to, relative to their size. Lastly,

Townsend's statement says that the velocity fields of the eddies should be somehow organized with respect to the wall, but does not prescribe any details of the shape of the flow. A schematic of the eddies in a turbulent flow through a channel is shown in Figure 1-2. The full height of the channel is  $2\delta$ , and this schematic only shows the lower half up to  $\delta$ . We show three layers of wall-attached eddies with white borders. In the smallest eddies shown here, it can be assumed that there are even smaller regions within, and vice versa for the larger eddies.

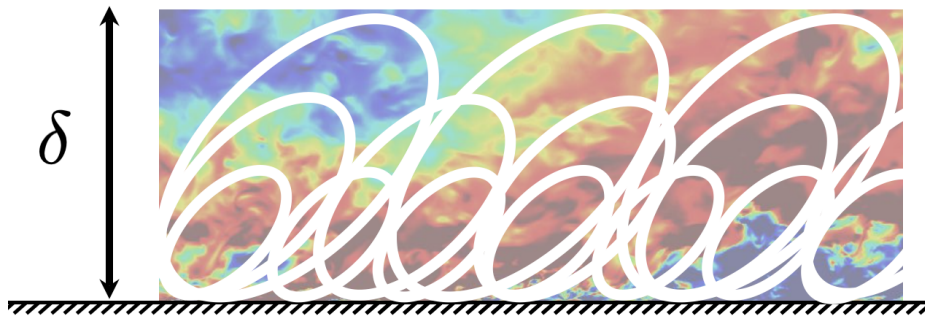


Figure 1-2: Visualization of eddies of turbulent channel flow.

Wall-bounded flows often show the development of boundary layers. Unlike channel flow, the boundary layer continually develops such that statistics depend on both the distance perpendicular to the boundary as well as the distance along the direction of the flow. Boundary layers are present over the surface of aerodynamic bodies. Early LES studies demonstrated inaccurate prediction of skin friction in equilibrium boundary layers [2]. Further, engineering applications often consist of complex geometries, which cause the imposition of pressure gradients onto these boundary layers. Early investigations on the onset of stall on airfoils demonstrated the need for increased grid refinement in areas of interest, particularly to capture laminar separation and turbulent reattachment [23].

### 1.3 Computational cost of simulating turbulence

Our overall goal is to simulate turbulent flows accurately, which means all scales of motion, from the largest energy-containing eddies to the smallest dissipative eddies defined by Kolmogorov, would be accounted for directly. DNS resolves all scales of motion, but is too computationally expensive for high-speed turbulent flows [37].

The computational cost of any simulation is mostly determined by the resolution requirements. We consider the case of isotropic turbulence. The side of the box domain  $\mathcal{L}$  must be large enough to comparably represent the largest energy-containing scales, while the grid spacing  $\Delta x$  must be small enough to resolve the smallest dissipative scales. The time step  $\Delta t$  to advance each realization of the solution must also conform to numerical stability requirements, usually imposed through the Courant number,  $\mathcal{U}\Delta t/\Delta x$ . We know that the smallest dissipative motions are characterized by the Kolmogorov scale  $\eta$ , so it can be deduced that the resolution therefore requires a grid spacing of at least  $\eta$  to capture these motions. This corresponds to the resolution of the small-scale motions requiring a sufficiently large maximum wave number  $\kappa_{\max}\eta$  [25]. Further, we know that the majority of discrete modes in wave number space is in the dissipative range, which is expensive to fully resolve through DNS considering the increasingly refined resolution required as Reynolds number is increased. Exploring new frameworks that attempt to match DNS accuracy while preserving computationally efficiency is an area of active research in the fluid dynamics community for a wide range of applications and a foundation of this work.

In LES, the energy-containing motions are resolved, while the effects of the unresolved modes are modeled. In general, for statistically three-dimensional flow, the evolution equations (such as the filtered Navier-Stokes equations in the case of LES) result in the well-known closure problem [29]. A set of equations with more unknowns than equations is unclosed. In turbulence, the set of statistics modeled by the evolution equations contain additional statistics to those considered in the set. Thus, the equations cannot be solved directly due to these additional terms. Instead, certain terms need to be modeled. For LES, these SGS terms that represent the smallest

dissipative motions that are unresolved are modeled. These terms are affiliated with the unresolved modes that are cut off during the filtering process, described in more detail in chapter 2. Developing and implementing new modeling approaches for these SGS terms is also an active area of research and explored in this work. We now motivate the connection of these new modeling techniques to our applications of interest, which often involve additional complexities introduced by compressibility effects in high-speed flow regimes.

## 1.4 Compressibility effects in high-speed turbulence

The foundation and motivation we have presented are critical in establishing fundamental properties and behavior of turbulent flows, as well as interest across academia and industry in developing improved modeling capabilities. We will now assess how the consideration of compressibility effects, which are relevant to high-speed applications we are interested in, complicates the theory and practice of turbulence modeling. Compressible flow is characterized by the non-dimensional parameter, the Mach number  $M = u/c$ , where  $u$  is the local flow velocity and  $c$  is the speed of sound.

We revisit isotropic turbulence, only now we consider the compressible case. Compressible isotropic turbulence still maintains spatial homogeneity [28]. Passot and Pouquet (1987) [42] were one of the first to study compressible isotropic turbulence using DNS under perfect gas assumptions for the two-dimensional case without modeling of the small scales. In the large scales, temporal exchanges between longitudinal and solenoidal modes of energy lead to a reduction of the decrease of Mach number as time progresses. With an initial supersonic flow, small scales are dominated by shocks. Later studies show that the initial conditions and forcing have a lasting effect on the evolution of the turbulence in the compressible case [28, 6]. Compressible turbulent flows in general have significant fluctuations in thermodynamic variables, such as entropy, temperature, pressure, and density. As the turbulent Mach number increases, the effects of acoustic nonlinearity become more considerable, such as shocklets [28]. Further, there are direct effects of compressibility on turbulent free shear

flows, such as the round jet, in the compressible mixing layer. Brown and Roshko (1974) [4] executed a high-speed mixing layer experiment between two streams of different gases. More large-scale eddies in the mixing layer that remained even for very high Reynolds numbers were observed. Further, it was demonstrated that the large reduction in the spreading rate was also a direct effect of compressibility [28]. Indirect effects of compressibility for free shear flows include changes in turbulence structure, including pressure fluctuations, pressure-strain correlation, and acoustic communication [14, 28].

For the compressible case, a fully developed compressible channel flow that is driven by a pressure gradient is not possible unless care is taken to remove the heat generated by viscous deformation [28]. Compressible channel flow has been studied using DNS and LES previously. Coleman et al. (1995) [8] performed DNS of a compressible supersonic turbulent channel flow at Mach numbers 1.5 and 3 based on bulk velocity and speed of sound at the wall at relatively low Reynolds numbers of order 30,000. It was found that the magnitude of the fluctuations of total temperature and pressure (i.e., thermodynamic properties) are much less than the mean profile values, implying that the dominant compressibility effect is on mean property variations, thus validating Markovin's hypothesis [34]. Yao and Hussain (2020) [70] performed DNS at Mach numbers 0.8 and 1.5 and Reynolds numbers ranging from 3,000 to 34,000. Although the streamwise Reynolds stress peak continuously increased with Mach number, this increase became smaller as the Reynolds number increased. Further, the compressibility contribution to the skin friction decreased with Reynolds number, suggesting that incompressible and compressible flows differ little at sufficiently high Reynolds number [70]. Chung and Pullin (2009) [7] performed WMLES of a turbulent channel flow with a near-wall SGS model based on wall-parallel filtering and wall-normal averaging of the streamwise momentum equation. Results demonstrated good agreement with DNS data from Hoyas and Jiménez (2006) for mean velocity profiles and acceptable second-order turbulence statistics. It was also demonstrated that subgrid-continued spectra agreed well with DNS down to Kolmogorov scales for the fully-developed region. Lee et al. (2013) [27] performed WMLES with coarse-grid

resolution near the wall and the mean wall shear stress as a boundary condition. The mean wall shear stress is determined by the log-law at each time step. It is shown that the logarithmic velocity profile and low-order turbulence statistics are accurately predicted. Accurate prediction of mean profiles for these studies is expected due to the law of the wall assumption. Still, it remains unclear if WMLES can reliably capture higher-order turbulence statistics, such as fluctuations [2]. More recent work by Park and Moin (2016) [39] demonstrated that the resolution requirement for predicting wall-pressure fluctuations is more stringent than that for predicting the velocity. Ideally, we want to develop a better SGS model for small-scale motions that can capture high-order turbulence statistics without needing an overly refined grid. Errors for WMLES are not well understood or well quantified, including errors due to spatial and temporal discretization, incomplete convergence, and physical modeling. NASA’s CFD Vision 2030 Study highlights the need for improvements in error quantification [53].

Studies of WMLES for high-speed flows, particularly those focused on accurately predicting heat transfer and skin friction, are still lacking. Law of the wall assumptions cause discrepancies for flows with substantial pressure gradients, near separation points where skin friction vanishes yet heat transfer remains [2]. These assumptions do not appear to greatly effect the prediction of the mean velocity profiles for flows with relatively lower pressure gradients. However, previous studies have demonstrated more amplified discrepancies in the prediction of the inner-layer temperature profiles and wall heat transfer [3, 20, 2].

The experimental aircraft X-59 Quiet SuperSonic Technology (QueSST) developed by Lockheed Martin at Skunk Works for NASA’s Low-Boom Flight Demonstrator project is one relevant and current high-speed example of interest to the CFD community [65]. The primary goal of NASA’s Low-Boom Flight Demonstrator project is to demonstrate feasibility of supersonic over-land flight at reduced loudness levels. So, accurate modeling of these quantities of interest, including shock waves and acoustic signatures, would accelerate certification by analysis efforts via CFD, such as with the X-59 QueSST, for example [66]. Current near-field CFD with RANS

models and subsequent atmospheric propagation to resolve noise signatures for the X-59 QueSST have been performed and published through the American Institute of Aeronautics and Astronautics (AIAA) Sonic Boom Prediction Workshop series [40]. However, RANS is often unable to accurately and reliably predict turbulent flows with significant regions of separation, which are often seen in high-speed applications with complex configurations, such as the X-59 QueSST [53]. We will assess the performance of WMLES for the X-59 QueSST in this work and make comparisons to existing RANS results in predicting statistical quantities of interest and overall computational cost.

Experiments of high-speed applications using WMLES are less abundant for many physical setups, from channel flow to flat-plate boundary layers to airfoils to realistic external aerodynamic applications [67]. So, our work will seek to address outstanding modeling challenges invoked by both compressibility effects introduced by high-speed flows and complex geometries of typical aerospace vehicles. These challenges culminate in accurately predicting thermodynamic and aerodynamic quantities of interest, such as heat flux at the wall or pressure gradients from shock waves.

## 1.5 Objectives and outline

The objectives for this thesis will be assessed strategically using two different high-speed applications: a compressible canonical channel flow and an external aerodynamic application, the Lockheed Martin Quiet SuperSonic Technology (QueSST) aircraft. We will address the following objectives throughout the work specific to the selected applications:

1. Quantify the error scaling properties for the compressible turbulent channel flow at high speeds at different flow conditions and grid resolutions.
2. Apply a new SGS modeling technique rooted in information theory to the channel flow and assess improvements in predicting quantities of interest.
3. Perform WMLES of a realistic external aerodynamic application, the X-59

QueSST, at cruise conditions.

4. Assess the performance and computational cost of traditional SGS models in predicting quantities of interest for the X-59 QueSST.

This thesis is organized as follows: the methodology of LES is presented in chapter 2, the canonical compressible channel flow is in chapter 3, the external aerodynamic application of the Lockheed Martin X-59 QueSST is in chapter 4, and conclusions and future work are consolidated in chapter 5. It follows that objectives (1) and (2) are addressed in chapter 3, and objectives (3) and (4) are addressed in chapter 4.



# Chapter 2

## Technical approach and methodology

### 2.1 Large-eddy simulation for compressible flows

#### 2.1.1 Conservation equations for compressible flow

The compressible Navier-Stokes equations that express the conservation of mass, momentum, and energy are used as a mathematical model for fluids written as

$$\frac{\partial \rho}{\partial t} + \frac{\partial \rho u_j}{\partial x_j} = 0, \quad (2.1)$$

$$\frac{\partial \rho u_i}{\partial t} + \frac{\partial \rho u_i u_j}{\partial x_j} = -\frac{\partial p}{\partial x_i} + \frac{\partial \sigma_{ij}}{\partial x_j}, \quad (2.2)$$

$$\frac{\partial \rho E}{\partial t} + \frac{\partial (\rho E + p) u_j}{\partial x_j} = \frac{\partial \sigma_{ij} u_i}{\partial x_j} - \frac{\partial Q_j}{\partial x_j}, \quad (2.3)$$

where  $t$  and  $x_i$  represent time and spatial coordinates [50]. The three components of the velocity vector are denoted by  $u_i$ . The total energy per unit mass  $E$  is defined by

$$\rho E = \frac{p}{\gamma - 1} + \frac{\rho u_i u_i}{2}, \quad (2.4)$$

where the density  $\rho$ , the pressure  $p$ , and the static temperature  $T$  are connected through the equation of state

$$p = \rho R T, \quad (2.5)$$

where the gas constant  $R = C_p - C_v$ . The specific heats at constant pressure  $C_p$  and constant volume  $C_v$  define  $\gamma = C_p/C_v$  as the ratio of specific heats. The heat flux  $Q_j$  is given by

$$Q_j = -\kappa \frac{\partial T}{\partial x_j}, \quad (2.6)$$

where  $\kappa = \mu C_p / \text{Pr}$  is the thermal conductivity, with  $\mu$  representing the dynamic viscosity. The Prandtl number  $\text{Pr}$  is the ratio of the kinematic viscosity  $\nu = \mu/\rho$  and thermal diffusivity  $\kappa/(\rho C_p)$ . The shear-stress tensor for a Newtonian fluid is given by Stokes' hypothesis,

$$\sigma_{ij} = 2\mu(T)S_{ij} - \frac{2}{3}\mu(T)\delta_{ij}S_{kk}, \quad (2.7)$$

where  $S_{ij}$  are the components of the rate-of-strain tensor written as

$$S_{ij} = \frac{1}{2} \left( \frac{\partial u_i}{\partial x_j} + \frac{\partial u_j}{\partial x_i} \right). \quad (2.8)$$

The variation of the dynamic viscosity  $\mu$  with temperature is approximated by a power law for Sutherland's law given by

$$\frac{\mu(T)}{\mu(T_0)} = \left( \frac{T}{T_0} \right)^{0.76}. \quad (2.9)$$

where  $T_0$  is the reference temperature. It is convenient to further derive the non-dimensional forms of these governing equations, as we will later assess how certain quantities of interest are coupled with different non-dimensional parameters that characterize the flow, such as Mach number and Reynolds number. We first derive the temperature form as used in the work by Moin et al. (1991) [38] from conservation

of energy. From the definition of total energy per unit mass, we show

$$E = \frac{p}{\rho(\gamma - 1)} + \frac{u_i u_i}{2}, \quad (2.10)$$

$$E = C_v T + \frac{u_i u_i}{2}, \quad (2.11)$$

$$E = e + \frac{u_i u_i}{2}, \quad (2.12)$$

where  $e$  is the internal energy per unit mass. We substitute to get

$$\frac{\partial \rho(e + u_i u_i/2)}{\partial t} + \frac{\partial(\rho(e + u_i u_i/2) + p)u_j}{\partial x_j} = \frac{\partial \sigma_{ij} u_i}{\partial x_j} - \frac{\partial Q_j}{\partial x_j}. \quad (2.13)$$

We use the conservation of momentum and the definition of internal energy  $e = C_v T$  to acquire the temperature form as

$$\frac{\partial}{\partial t}(\rho C_v T) + \frac{\partial}{\partial x_j}(\rho u_j C_v T) = -p \frac{\partial u_j}{\partial x_j} + \sigma_{ij} \frac{\partial u_i}{\partial x_j} - \frac{\partial Q_j}{\partial x_j} \quad (2.14)$$

We can nondimensionalize the conservation equations by reference quantities  $U_0$ , length  $l$ , density  $\rho_0$ , and dynamic viscosity  $\mu_0$  to have resulting conservation equations that include dimensionless quantities. We use this approach with the conservation of momentum to get

$$\frac{\partial \rho u_i}{\partial t} + \frac{\partial \rho u_i u_j}{\partial x_j} = -\frac{\partial p}{\partial x_i} + \frac{\partial \sigma_{ij}}{\partial x_j}, \quad (2.15)$$

⋮

$$\frac{\partial \rho u_i}{\partial t} + \frac{\partial \rho u_i u_j}{\partial x_j} = -\frac{\partial p}{\partial x_i} + \frac{1}{\text{Re}} \frac{\partial \sigma_{ij}}{\partial x_j}, \quad (2.16)$$

where the Reynolds number  $\text{Re} = U_0 l \rho_0 / \mu_0$ . This shows a link between Reynolds number and velocity through the conservation of momentum. We can follow analog-

gously for the temperature form of the conservation of energy to arrive at

$$\frac{\partial}{\partial t}(\rho C_v T) + \frac{\partial}{\partial x_j}(\rho u_j C_v T) = -p \frac{\partial u_j}{\partial x_j} + \sigma_{ij} \frac{\partial u_i}{\partial x_j} - \frac{\partial Q_j}{\partial x_j}, \quad (2.17)$$

⋮

$$\frac{\partial}{\partial t}(\rho C_v T) + \frac{\partial}{\partial x_j}(\rho u_j C_v T) = -\gamma M^2(\gamma - 1)p \frac{\partial u_j}{\partial x_j} + \frac{\gamma M^2(\gamma - 1)}{Re} \sigma_{ij} \frac{\partial u_i}{\partial x_j} - \frac{\gamma}{RePr} \frac{\partial Q_j}{\partial x_j}, \quad (2.18)$$

where the Mach number  $M = U_0/a_0$ . The reference speed of sound  $a_0 = \sqrt{\gamma RT_0}$ , with reference temperature  $T_0$ . This shows a strong link between Mach number and temperature. We also see dependence on the Reynolds number again and the Prandtl number on the heat flux term. The full derivation of the non-dimensional forms of the compressible conservation equations is in Appendix A. We can take this formulation for compressible flows to acquire the governing equations for LES.

### 2.1.2 Filtering operator

Scales are separated using a scale high-pass filter, corresponding to a low-pass filter in frequency. The mathematical representation in physical space manifests as a convolution product. The resolved part  $\bar{\phi}(\mathbf{x}, t)$  of some space-time variable  $\phi(\mathbf{x}, t)$  is defined as

$$\bar{\phi}(\mathbf{x}, t) = \frac{1}{\Delta} \int_{-\infty}^{\infty} \int_{-\infty}^{\infty} G\left(\frac{\mathbf{x} - \xi}{\Delta}, t - t'\right) \phi(\xi, t') dt' d^3\xi, \quad (2.19)$$

where the convolution kernel  $G$  is dependent on the filter and is associated with the cutoff scale in space  $\Delta$  and the cutoff scale in time  $\tau_c$  [50]. This relation is commonly denoted symbolically by  $\bar{\phi} = G \star \phi$ . The dual definition in Fourier space is acquired by multiplying the spectrum  $\hat{\phi}(\mathbf{k}, \omega)$  of  $\phi(\mathbf{x}, t)$  by the transfer function  $\hat{G}(\mathbf{k}, \omega)$  of the kernel  $G(\mathbf{x}, t)$  to get  $\hat{\bar{\phi}}(\mathbf{k}, \omega) = \hat{G}(\mathbf{k}, \omega)\hat{\phi}(\mathbf{k}, \omega)$ , with an analogous symbolic form  $\hat{\bar{\phi}} = \hat{G}\hat{\phi}$ . The hat terms  $(\hat{\cdot})$  represent the Fourier transform. In Fourier space, it follows that the spatial cutoff length  $\Delta$  is associated to the cutoff wave number  $k_c$  for

wave number  $\mathbf{k}$ . The spatial cutoff time  $\tau_c$  is associated with the cutoff frequency  $\omega_c$  for frequency  $\omega$  [50]. The non-resolved part  $\phi'(\mathbf{x}, t)$  of  $\phi(\mathbf{x}, t)$  is defined as

$$\phi'(\mathbf{x}, t) = \phi(\mathbf{x}, t) - \bar{\phi}(\mathbf{x}, t) \quad (2.20)$$

and written in symbolic form as  $\phi' = (1 - G) \star \phi$  [50]. The fundamental properties of the filtering operator are consistency, linearity satisfied by the convolution form, and commutation with differentiation which is satisfied only if the domain is unbounded and if the convolution kernel is homogeneous [50]. For wall-bounded flows, the cutoff length must be varied in order to adapt the filter to the solution structure. This adaptation is necessary because this filter lengthscale should decrease close to the wall to capture the smallest active scales. Spatial filtering implies a consequent temporal filtering since the governing equations demonstrate an association between a characteristic timescale and lengthscale [43, 50]. Suppressing the spatial scales corresponding to wave numbers that are greater than  $k_c$  therefore implies the suppression of frequencies higher than the cutoff frequency  $\omega_c$ . Convolution filters commonly used for performing the spatial scale separation include the Box filter, the Gaussian filter, and the sharp cutoff filter. For example, a sharp cutoff filter in wave space was used to define  $G$  by Moin (1991) [38] as

$$G_i(k_i) = \begin{cases} 1 & k_i \leq \pi/\Delta_i \\ 0 & \text{else} \end{cases} \quad (2.21)$$

where  $G_i$  is the Fourier coefficient of the filter function in the  $i^{\text{th}}$  direction and  $\Delta_i$  is the respective filter width. Here, the analytical filter represented by a convolution product is then used for expressing the filtered governing equations. There are additional filtering classes associated to the computational grid and numerical scheme.

## Favre filtering

Employing a change of variable in which filtered variables are weighted by the density is common for LES of compressible flows [50]. This change of variables is written as

$$\overline{\rho\phi} = \bar{\rho}\tilde{\phi}, \quad (2.22)$$

where  $\phi$  is a flow variable of interest. This variable can be decomposed into a low frequency part  $\tilde{\phi}$  and a high frequency part  $\phi''$  as

$$\phi = \tilde{\phi} + \phi''. \quad (2.23)$$

The  $(\tilde{\cdot})$  operator is linear but does not commute with the derivative operators in space and time. Mathematically,

$$\frac{\partial \tilde{\phi}}{\partial x_j} \neq \frac{\partial \tilde{\phi}}{\partial x_j}, \quad (2.24)$$

$$\frac{\partial \tilde{\phi}}{\partial t} \neq \frac{\partial \tilde{\phi}}{\partial t}. \quad (2.25)$$

If the  $(\bar{\cdot})$  is a Reynolds operator, satisfying linearity and averaging in time, we can say

$$\overline{\rho\phi''} = 0, \quad (2.26)$$

$$\bar{\phi} - \tilde{\phi} = \bar{\phi}'' = -\frac{\rho'\phi'}{\bar{\rho}} = -\frac{\overline{\rho'\phi''}}{\bar{\rho}}. \quad (2.27)$$

This change of variable is consistent with the idea of Favre averaging [12]. The connection is that we have a filtering here expressed in terms of Favre variables via a change of variable. As we will see, coupled terms such as  $\overline{\rho u_i}$  present in the filtered continuity equation can be decomposed nicely with this operator. Without Favre filtering, the transformation from  $\overline{\rho u_i}$  to  $\bar{\rho} \bar{u}_i$  would result in an additional SGS term to be modeled. We now revisit the conservation equations and apply the filtering operator to acquire the governing equations for LES.

### 2.1.3 Governing equations of large-eddy simulation

The conservation equations in a statistically averaged form can be obtained by introducing a decomposition of the flow variables and taking the statistical average [28]. We apply a spatial filter to the conservation equations to obtain

$$\frac{\partial \bar{\rho}}{\partial t} + \frac{\partial \bar{\rho} \bar{u}_j}{\partial x_j} = 0, \quad (2.28)$$

$$\frac{\partial \bar{\rho} \bar{u}_i}{\partial t} + \frac{\partial \bar{\rho} \bar{u}_i \bar{u}_j}{\partial x_j} = -\frac{\partial \bar{p}}{\partial x_i} + \frac{\partial \bar{\sigma}_{ij}}{\partial x_j}, \quad (2.29)$$

$$\frac{\partial}{\partial t} (\bar{\rho} C_v \bar{T}) + \frac{\partial}{\partial x_j} (\bar{\rho} \bar{u}_j C_v \bar{T}) = -p \frac{\partial \bar{u}_j}{\partial x_j} + \bar{\sigma}_{ij} \frac{\partial \bar{u}_i}{\partial x_j} - \frac{\partial \bar{Q}_j}{\partial x_j}. \quad (2.30)$$

We use Favre filtering to decouple the following terms as

$$\bar{\rho} \bar{u}_i = \bar{\rho} \tilde{u}_i, \quad (2.31)$$

$$\bar{\rho} \bar{u}_i \bar{u}_j = \bar{\rho} \tilde{u}_i \tilde{u}_j = \bar{\rho} \tilde{u}_i \tilde{u}_j + \bar{\rho} (\tilde{u}_i \tilde{u}_j - \tilde{u}_i \tilde{u}_j), \quad (2.32)$$

$$\bar{\rho} \bar{u}_i \bar{T} = \bar{\rho} \tilde{u}_i \tilde{T} = \bar{\rho} \tilde{u}_i \tilde{T} + \bar{\rho} (\tilde{u}_i \tilde{T} - \tilde{u}_i \tilde{T}), \quad (2.33)$$

unveiling the SGS terms that must be subsequently modeled. Upon substitution,

$$\frac{\partial \bar{\rho}}{\partial t} + \frac{\partial \bar{\rho} \tilde{u}_j}{\partial x_j} = 0, \quad (2.34)$$

$$\frac{\partial \bar{\rho} \tilde{u}_i}{\partial t} + \frac{\partial \bar{\rho} \tilde{u}_i \tilde{u}_j}{\partial x_j} = -\frac{\partial \bar{p}}{\partial x_i} + \frac{1}{\text{Re}} \frac{\partial \bar{\sigma}_{ij}}{\partial x_j} - \frac{\partial \tau_{ij}}{\partial x_j}, \quad (2.35)$$

$$\begin{aligned} \frac{\partial}{\partial t} (\bar{\rho} C_v \tilde{T}) + \frac{\partial}{\partial x_j} (\bar{\rho} \tilde{u}_j C_v \tilde{T}) + \frac{\partial q_i}{\partial x_j} &= -\gamma M^2 (\gamma - 1) \bar{p} \frac{\partial \tilde{u}_j}{\partial x_j} \\ &\quad + \frac{\gamma M^2 (\gamma - 1)}{\text{Re}} \bar{\sigma}_{ij} \frac{\partial \bar{u}_i}{\partial x_j} - \frac{\gamma}{\text{RePr}} \frac{\partial \bar{Q}_j}{\partial x_j}. \end{aligned} \quad (2.36)$$

The effect of the small-scale motions on the resolved eddies are present in the SGS stress tensor  $\tau_{ij}$  and SGS heat flux vector  $q_i$ :

$$\tau_{ij} = \bar{\rho} (\tilde{u}_i \tilde{u}_j - \tilde{u}_i \tilde{u}_j) \quad (2.37)$$

$$q_i = \bar{\rho} (\tilde{u}_i \tilde{T} - \tilde{u}_i \tilde{T}) \quad (2.38)$$

The objective of LES is to model the SGS terms as functions of known filtered quantities and model parameters.

## 2.2 Existing subgrid-scale models

### 2.2.1 Dynamic Smagorinsky model

Most SGS stress models are based on an eddy viscosity assumption. In the most common model developed by Smagorinsky (1963) [54], the eddy viscosity  $\nu_T$  is acquired by assuming that the small scales are in equilibrium such that energy production and dissipation are in balance. The expression is

$$\nu_T = (C_s \Delta)^2 |\bar{S}|, \quad (2.39)$$

where  $\Delta$  is the filter width proportional to the grid size,  $C_s$  is the Smagorinsky constant, and  $|\bar{S}|$  is the magnitude of the large-scale strain-rate tensor. However, consequent work revealed that it is not possible to model all regimes of flow effectively with a single, universal constant. Germano et al. (1991) [17] developed a dynamic SGS stress model that locally calculates the eddy viscosity coefficient to reflect the state of the flow more intentionally by sampling the smallest resolved scales to model the subgrid scales.

We revisit the filtering operator to formulate the dynamic Smagorinsky (DSM) model. We let the typical grid filter  $\bar{G}$  be defined as  $\bar{f} = \bar{G} \star f$  and extend over the entire computational domain. We define the test filter  $\check{G}$  as  $\check{f} = \check{G} \star f$ , where the filter width of the test filter is assumed to be larger than that of the grid filter. In other words, the test filter corresponds to a coarser mesh than the grid filter. We also let  $\check{\bar{G}} = \check{G} \bar{G}$ . In applying  $\check{\bar{G}}$  to the conservation equations of motion, the filtered compressible Navier-Stokes equations result in the SGS stress now being

$$T_{ij} = \bar{\rho} \left( \widetilde{u_i u_j} - \check{\bar{u}_i} \check{\bar{u}_j} \right), \quad (2.40)$$

and we let the resolved turbulent stress be defined as

$$\mathcal{L}_{ij} = \bar{\rho} \left( \widetilde{\bar{u}_i \bar{u}_j} - \widetilde{\bar{u}_i} \widetilde{\bar{u}_j} \right), \quad (2.41)$$

which represent the contribution of the Reynolds stresses by the small resolved scales with lengths in between the grid filter width and the test filter width. These quantities are related through

$$\mathcal{L}_{ij} = T_{ij} - \tau_{ij}. \quad (2.42)$$

Thus, this work by Germano et al. (1991) [17] related the explicitly calculated resolved turbulent stress to the SGS stresses at the test and grid levels. This can be used to derive more accurate SGS stress models by adjusting the Smagorinsky coefficient depending on the instantaneous state of the flow. Assuming the Smagorinsky model is used to parametrize  $T_{ij}$  and  $\tau_{ij}$ , the dynamic Smagorinsky model is given by

$$m_{ij} = \frac{\langle \mathcal{L}_{kl} \bar{S}_{kl} \rangle}{\left( \frac{\check{\Delta}}{\bar{\Delta}} \right)^2 \langle |\bar{S}| \check{\bar{S}}_{mn} \bar{S}_{mn} \rangle - \langle \widetilde{|\bar{S}| \bar{S}_{pq} \bar{S}_{pq}} \rangle} |\bar{S}| \bar{S}_{ij} \quad (2.43)$$

where  $m_{ij}$  is the model for the anisotropic part of  $\tau_{ij}$  [17].

### 2.2.2 Vreman model

The implementation of the dynamic Smagorinsky model requires explicit filtering operations, ensemble averaging, and additional clipping to prevent an unstable eddy viscosity. Thus, extension to complex flows is not trivial. Vreman (2004) [61] proposed a new eddy viscosity for the following model

$$\tau_{ij} = -2\nu_e S_{ij} + \tau_{kk} \delta_{ij}/3. \quad (2.44)$$

The eddy viscosity is defined by

$$\nu_e = c \sqrt{\frac{B_\beta}{\alpha_{ij}\alpha_{ij}}}, \quad (2.45)$$

where  $\alpha_{ij} = \partial \tilde{u}_j / \partial x_i$ ,  $\beta_{ij} = \Delta_m^2 \alpha_{mi} \alpha_{mj}$ , and  $B_\beta = \beta_{11}\beta_{22} - \beta_{12}^2 + \beta_{11}\beta_{33} - \beta_{13}^2 + \beta_{22}\beta_{33} - \beta_{33}^2$ . The model constant  $c \approx 2.5C_s^2$ , where  $C_s$  is the Smagorinsky constant. The matrix  $\alpha$  represents the derivatives of the filtered velocity. The tensor  $\beta$  is proportional to the gradient model in its general anisotropic form. The model is invariant under a rotation of the coordinate axes. The idea of the model stems from algebraic properties of the theoretical subgrid dissipation [61].

## 2.3 Novel information-preserving model

### 2.3.1 Preliminary concepts of information theory

Lastly, we introduce a novel SGS modeling technique. This modeling approach was validated by Lozano-Durán and Arranz (2022) [31] for homogeneous turbulence, and it will be applied to the channel flow as in the original work by Williams and Lozano-Durán (2022) [67]. We introduce preliminary concepts of information theory required to formulate the problem of modeling. Consider the discrete random variable  $X$  taking values equal to  $x$  with probability mass function  $p(x) = \Pr\{X = x\}$  over the finite set of outcomes  $\mathcal{X}$  of  $X$ . The information of observing the event  $X = x$  is defined as [52]

$$\mathcal{I}(x) = -\log_2[p(x)]. \quad (2.46)$$

The units of  $\mathcal{I}(x)$  are bits, as set by the base chosen for this case. If we consider tossing a fair coin such that  $p(\text{heads}) = p(\text{tails}) = 0.5$ , the information of getting heads after one flip is  $\mathcal{I}(\text{heads}) = -\log_2(0.5) = 1$  bit. In other words, observing the outcome of flipping a fair coin provides one bit of information. If the coin is completely biased toward heads, no information is gained since the outcome was already known before flipping the coin. Thus, information is the statistical notion of how unlikely

it is to observe an event. The information  $\mathcal{I}(x)$  is the number of bits required to unambiguously determine the state  $x$ .

The average information in  $X$  is given by the expectation  $\langle \cdot \rangle$  over all the possible outcomes, defined as

$$H(X) = \langle \mathcal{I}(x) \rangle = \sum_{x \in \mathcal{X}} -p(x) \log_2[p(x)] \geq 0. \quad (2.47)$$

Equation (2.47) is referred to as the Shannon entropy [52]. In flipping a fair coin  $n$  times, the entropy  $H = -\sum 0.5^n \log_2(0.5^n) = n$  bits. Thus, Eq. (2.47) corresponds to the minimum average number of bits needed to encode a source of  $n$  states with probability distribution  $p$  [52]. So,  $H$  is zero when the process is completely deterministic, with no uncertainty in the outcome.

Interpreting information in the form of bits in terms of uncertainty is used in the formulation of the Kullback-Leibler (KL) divergence. If we consider two probability mass distributions,  $p(x)$  and  $q(x)$ , the KL divergence is defined as

$$\text{KL}(p, q) = \sum_{x \in \mathcal{X}} p(x) \log \frac{p(x)}{q(x)}, \quad (2.48)$$

which is a measure of the average number of bits required to recover  $p(x)$  using the information in  $q(x)$ . The KL divergence also represents the information lost when  $q(x)$  is used to approximate  $p(x)$ . Note that Eq.(2.48) is an extension of Eq.(2.47) and can be referred to as relative entropy [19]. Thus, the KL divergence is equal to zero when the probability mass distributions are exactly the same. These definitions are applicable to scalar random variables but can be generalized to a vector of random variables with a joint probability.

### 2.3.2 Information theory for modeling

The goal of modeling is to preserve the maximum amount of useful information from the original system [31]. Consider a dynamical system governed by

$$\mathbf{q}^{n+1} = \mathbf{f}(\mathbf{q}^n), \quad (2.49)$$

where we have  $\mathbf{q}^n = [q_1^n, \dots, q_j^n, \dots, q_N^n]$  as the state vector at time  $t_n$  with  $N$  being the total number of degrees of freedom in Eq. (2.49). We define  $\mathbf{f}$  as the function that advances the state of the system through time. We consider the partition of the phase-space of the full system

$$\mathbf{q}^n = [\tilde{\mathbf{q}}^n, \mathbf{q}'^n]. \quad (2.50)$$

We aim to model the subset of the phase-space denoted by  $\tilde{\mathbf{q}}^n = [q_1^n, \dots, q_{\tilde{N}}^n]$  in Eq. (2.50), where  $\tilde{N} < N$  are the degrees of freedom of the model. Since  $\tilde{\mathbf{q}}^n$  is the state to be modeled,  $\mathbf{q}'^n$  represents the inaccessible degrees of freedom that must be accounted for by the model. The dynamics of the modeled state is governed by

$$\tilde{\mathbf{q}}^{n+1} = \tilde{\mathbf{f}}(\tilde{\mathbf{q}}^n, \mathbf{q}'^n), \quad (2.51)$$

where  $\tilde{\mathbf{f}}$  are the components of  $\mathbf{f}$  corresponding to the states  $\tilde{\mathbf{q}}^n$ . We now consider a model with access to the information contained in  $\tilde{\mathbf{q}}^n$  but not to the information in  $\mathbf{q}'^n$ . The governing equation for the model is denoted by

$$\tilde{\mathbf{q}}_{\text{model}}^{n+1} = \tilde{\mathbf{f}}_{\text{model}}(\tilde{\mathbf{q}}^n), \quad (2.52)$$

where  $\tilde{\mathbf{q}}_{\text{model}}^{n+1}$  is the model prediction, which does not need to match the exact solution  $\tilde{\mathbf{q}}^{n+1}$  from Eq. (2.51). We want to find  $\tilde{\mathbf{f}}_{\text{model}}$  that predicts the future state to within some error  $\varepsilon$  defined as

$$\|\tilde{\mathbf{q}}_{\text{model}}^{n+1} - \tilde{\mathbf{q}}^{n+1}\| \leq \varepsilon, \quad (2.53)$$

where  $\|\cdot\|$  is the  $L_1$  norm. This error constraint can be relaxed to

$$\|p(\tilde{\mathbf{q}}_{\text{model}}^{n+1}) - p(\tilde{\mathbf{q}}^{n+1})\| \leq \varepsilon, \quad (2.54)$$

where  $p(\tilde{\mathbf{q}}^{n+1})$  is the true probability distribution of the system state and  $p(\tilde{\mathbf{q}}_{\text{model}}^{n+1})$  is the probability distribution of the model state. Note that this constraint is weaker in that it is possible that a model can replicate the statistics of the actual state, yet the dynamics of the model may not coincide with the true state. Nevertheless, the error defined by Eq. (2.54) yields an estimated upper bound for the expectation of the modeling error of probabilities.

We reintroduce the KL divergence between  $p(\tilde{\mathbf{q}}^{n+1})$  and  $p(\tilde{\mathbf{q}}_{\text{model}}^{n+1})$  as

$$\text{KL}(\tilde{\mathbf{q}}^{n+1}, \tilde{\mathbf{q}}_{\text{model}}^{n+1}) = \sum p(\tilde{\mathbf{q}}^{n+1}) \log \frac{p(\tilde{\mathbf{q}}^{n+1})}{p(\tilde{\mathbf{q}}_{\text{model}}^{n+1})}, \quad (2.55)$$

with  $\text{KL}(\tilde{\mathbf{q}}^{n+1}, \tilde{\mathbf{q}}_{\text{model}}^{n+1}) = 0$  if and only if the model predictions are statistically identical to those from the original system. It can be shown via the Pinsker's inequality [64] that

$$\text{KL}(\tilde{\mathbf{q}}^{n+1}, \tilde{\mathbf{q}}_{\text{model}}^{n+1}) \geq \frac{1}{2 \ln 2} \|p(\tilde{\mathbf{q}}_{\text{model}}^{n+1}) - p(\tilde{\mathbf{q}}^{n+1})\|^2. \quad (2.56)$$

Substituting to reintroduce the prescribed error for the upper bound gives

$$\text{KL}(\tilde{\mathbf{q}}^{n+1}, \tilde{\mathbf{q}}_{\text{model}}^{n+1}) \geq \frac{\varepsilon^2}{2 \ln 2}. \quad (2.57)$$

Equation (2.57) therefore yields a connection between information loss and probabilistic model performance. The model  $\tilde{\mathbf{f}}_{\text{model}}$  that we seek will minimize Eq. (2.55), thus containing the coherent information in the data, while disregarding the incoherent noise. This formulation can be extended to the problem of modeling for turbulent flows.

### 2.3.3 Information-preserving model

The previous formulation can therefore be applied in devising an SGS model for LES. The objective of LES is to model the SGS tensor as a function of known filtered quantities defined by

$$\tau_{ij} = \tau_{ij}(\bar{S}_{ij}, \bar{\Omega}_{ij}, \bar{\Delta}; \boldsymbol{\theta}), \quad (2.58)$$

where  $\bar{S}_{ij}$  and  $\bar{\Omega}_{ij}$  are the filtered rate-of-strain and rate-of-rotation tensors, respectively, and  $\boldsymbol{\theta}$  are model parameters.

The map  $\mathbf{f}$  in Eq. (2.49) corresponds to a discrete version of the Navier-Stokes equations, resolving all the space and time scales. The state vector  $\mathbf{q}^n$  is given by the discretization of the velocities and pressure in a grid fine enough to capture all the relevant scales of motion. The map  $\tilde{\mathbf{f}}_{\text{model}}$  for the model is derived from the discretization of Eq. (2.49). The model state vector  $\tilde{\mathbf{q}}_{\text{model}}^n$  therefore corresponds to the filtered velocities and pressure.

We start from the general expansion of the SGS tensor in terms of  $\bar{S}_{ij}$  and  $\bar{\Omega}_{ij}$  proposed by Lund and Novikov (1992) [33]. Retaining the two leading terms for the functional form considered for the SGS stress tensor results in

$$\tau_{ij} - \frac{1}{3}\tau_{kk}\delta_{ij} = \theta_1\bar{\Delta}^2\bar{S}_{ij}\sqrt{\bar{S}_{nm}\bar{S}_{nm}} + \theta_2\bar{\Delta}^2(\bar{S}_{ik}\bar{\Omega}_{kj} - \bar{\Omega}_{ik}\bar{S}_{kj}), \quad (2.59)$$

where  $\delta_{ij}$  is the Kronecker delta, and  $\theta_1$  and  $\theta_2$  are modeling parameters to be determined. We also introduce the interscale energy transfer and viscous dissipation in the case of LES at the filter cutoff  $\bar{\Delta}$  given by

$$\bar{\Gamma} = (\bar{u}_i\bar{u}_j - \bar{u}_i\bar{u}_j)\bar{S}_{ij} - 2\nu\bar{S}_{ij}\bar{S}_{ij} + \tau_{ij}\bar{S}_{ij}. \quad (2.60)$$

We invoke the modeling assumption that the information content content of  $p(\bar{\Gamma}_1)$  must be equal to the information content of  $p(\bar{\Gamma}_2\gamma)$ , where  $\bar{\Gamma}_1$  and  $\bar{\Gamma}_2$  are  $\bar{\Gamma}$  at scale  $\bar{\Delta}_1$  and  $\bar{\Delta}_2$ , respectively, and  $\gamma = (\bar{\Delta}_1/\bar{\Delta}_2)^{2/3}$  is a scaling factor. The model aims at minimizing the information lost when  $p(\bar{\Gamma}_1)$  is used to approximate  $p(\bar{\Gamma}_2\gamma)$  in the LES solution. Thus, it follows that the model is formulated using the KL divergence,

ensuring that the average information required for reconstructing  $p(\bar{\Gamma}_2\gamma)$  is minimum given the information in  $p(\bar{\Gamma}_1)$  given by

$$\boldsymbol{\theta} = \arg \min_{\boldsymbol{\theta}'} \text{KL}(\bar{\Gamma}_2\gamma, \bar{\Gamma}_1), \quad (2.61)$$

where  $\boldsymbol{\theta} = (\theta_1, \theta_2)$  from Eq. (2.59). This model will be referred to as the information-preserving (IP) SGS model.

## 2.4 Wall-modeled large-eddy simulation

At high Reynolds numbers, LES is complemented by a wall model which accounts for the smallest energy eddies in the vicinity of the wall, referred to as WMLES. Figure 2-1 shows a schematic for the wall model used to compute the channel flow with the grid. Given an instantaneous velocity  $u_i$ , pressure  $p$ , and temperature  $T$  at height  $y = h_{wm}$  above the wall, the instantaneous wall shear stress vector  $\tau_w$  and heat flux vector  $q_w$  are estimated.

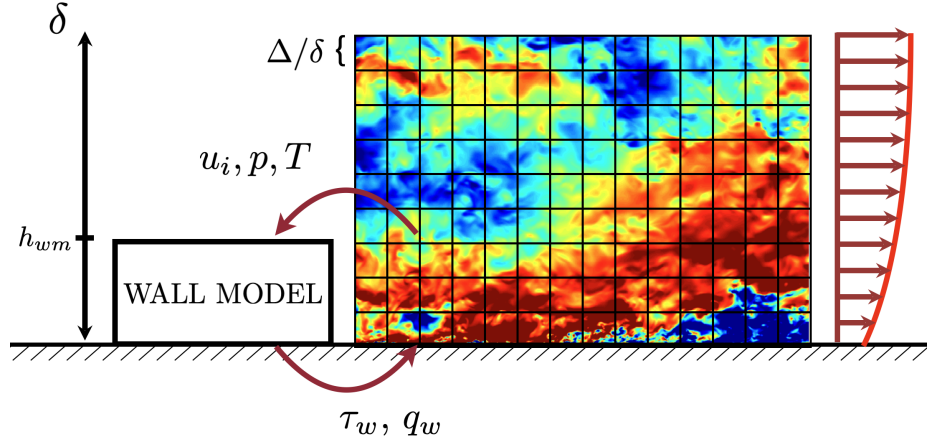


Figure 2-1: Wall model for channel flow.

In a stress-based WMLES approach, the computational grid is coarse in the wall-normal direction, requiring a wall shear stress and heat flux to be provided as a boundary condition along with the regular no-slip boundary condition. Stress-based WMLES is further divided into equilibrium and nonequilibrium models. The equi-

librium wall model neglects nonequilibrium effects such as acceleration and pressure gradient. Thus, this model has been shown to work well for canonical wall-bounded flows such as channel flow [21].

For our work, a compressible equilibrium wall-stress model (EQWM) is used to overcome the restrictive grid-resolution requirements to resolve the small-scale flow motions near the wall. The wall stress is obtained from an algebraic wall model derived from the integration of the one-dimensional equilibrium stress model along the wall-normal direction. The EQWM is an ODE-based wall-stress-model with simplified momentum and total energy equations given by [26]

$$\frac{d}{dy} \left[ (\mu_{wm} + \mu_{t,wm}) \frac{du_{wm}}{dy} \right] = 0, \quad (2.62a)$$

$$\frac{d}{dy} \left[ (\mu_{wm} + \mu_{t,wm}) u_{wm} \frac{du_{wm}}{dy} + C_p \left( \frac{\mu_{wm}}{\text{Pr}_{wm}} + \frac{\mu_{t,wm}}{\text{Pr}_{t,wm}} \right) \frac{dT_{wm}}{dy} \right] = 0, \quad (2.62b)$$

where  $\mu$  is the dynamic viscosity,  $\text{Pr}$  is the Prandtl number, the subscript “ $t$ ” denotes a turbulent quantity, and the subscript  $wm$  denotes a wall model quantity. The eddy viscosity is taken from the mixing-length model as

$$\mu_{t,wm} = \kappa \rho_{wm} y \sqrt{\frac{\tau_{w,wm}}{\rho_{wm}}} \left[ 1 - \exp \left( \frac{-y^+}{A^+} \right) \right]^2, \quad (2.63)$$

where  $\tau_w$  is the instantaneous wall stress. The model parameters  $\kappa$ ,  $\text{Pr}$ , and  $A^+$  are constants. Constants in plus units (+) are normalized by the friction velocity. More details on this wall model can be found in the work by Larsson and Kawai (2010) [26]. Effectively, given an instantaneous velocity at some height above the wall, the model estimates the instantaneous wall stress and heat flux. The no-slip boundary condition at the walls is replaced instead by a wall-stress boundary condition. The wall is assumed to be isothermal. The equations are solved for  $u_{wm}$  and  $T_{wm}$  in an overlapping layer between  $y = 0$  and  $y = h_{wm}$ . The additional wall model quantities are computed from the solution to the wall-stress model, not from the LES solution. The boundary condition at  $y = 0$  is the adiabatic no-slip condition. At  $y = h_{wm}$ ,  $u_{wm}$  and  $T_{wm}$  are imposed from the instantaneous LES solution. After solving,  $\tau_{w,wm}$

and  $q_{w,\text{wm}}$  at the wall are computed directly and returned to the LES as a boundary condition at the wall [22].

## 2.5 Numerical solver

The simulations are performed using WMLES with the code charLES from Cascade Technologies (Cadence). The validation of the algorithm can be found in Fu et al. (2020) [15]. The solver integrates the filtered Navier-Stokes equations using a second-order accurate finite volume formulation. The numerical discretization relies on a flux formulation that is approximately entropy preserving in the inviscid limit, thereby limiting the amount of numerical dissipation added into the calculation. The time integration is performed with a third-order Runge-Kutta explicit method. The mesh generator is based on a Voronoi hexagonal close packed point-seeding method which automatically builds high-quality meshes for arbitrarily complex geometries with minimal user input. An EQWM is used along with an SGS model to capture small-scale motions away from the wall.

## 2.6 Supercomputing resources

All simulations in this work are performed using high-performance computing resources provided by the MIT Supercloud. The MIT Supercloud is a collaboration with MIT Lincoln Laboratory on a shared facility that is optimized for streamlining open research [46]. The system is designed to support work that requires significant compute or memory resources. The system has 32,000 CPU cores and 448 Nvidia Volta GPUs in total. The Lincoln Laboratory Supercomputing Center connects to the Massachusetts Green High Performance Computing Center (MGHPCC), and system specifications are outlined in Table 2.1.

Table 2.1: MGHPCC TX-E1 specifications

Processor	Intel Xeon Platinum 8260
Nodes	480
Node RAM	192 GB
CPUs/node	2 × 24
RAM/core	4 GB
Local disk	4.4 TB

# Chapter 3

## Canonical case: compressible turbulent channel flow

### 3.1 Objectives

Error scaling properties of WMLES of compressible wall-bounded turbulent flows are investigated. The statistical quantities of interest investigated are the mean velocity profile, mean temperature profile, heat flux at the wall, and skin friction coefficient at the wall. It is assumed that errors scale as  $(\Delta/\delta)^\alpha \text{Re}^\gamma M^\beta$ , where  $\Delta$  is the characteristic grid resolution,  $\text{Re}$  is the bulk Reynolds number,  $\delta$  is the channel half-height, and  $M$  is the Mach number. Then, the problem of modeling for turbulent flows is investigated within the framework of information theory as in Williams and Lozano-Durán [67]. WMLES is conducted using an information-preserving (IP) subgrid-scale (SGS) model and compared to traditional models. Refer to the previous chapter for the formulation of the IP SGS model. It is found that the IP SGS model matches or exceeds the accuracy of the DSM SGS model when compared to DNS data for the compressible channel.

### 3.2 Physical and computational setup

Figure 3-1 shows a schematic for channel flow, where  $\langle u \rangle$  is the mean velocity along homogeneous directions and time. The channel domain is defined by the channel half-height  $\delta$ , and the domain size is  $6\pi\delta \times 2\delta \times 2\pi\delta$  in the  $x$ ,  $y$ , and  $z$  directions, respectively. The velocity of the flow field is  $u$  in  $x$ ,  $v$  in  $y$ , and  $w$  in  $z$ . The simulations are performed in a canonical compressible channel flow at the bulk Reynolds numbers  $Re = \rho_b u_b \delta / \mu_w = 15K, 17K, 24K$ , and  $34K$  and bulk Mach numbers  $M = u_b / \sqrt{\gamma R T_w} = 0.8, 1.5$ , and  $3.0$ . The bulk Reynolds number is based on the bulk density  $\rho_b$ , bulk velocity  $u_b$ ,  $\delta$ , and wall viscosity  $\mu_w$ . The bulk Mach number is based on  $u_b$  and wall temperature  $T_w$ . Results are compared to DNS data from Coleman et al. [8]. The DNS results are generated by adjusting the body force such that the total mass flux through the channel remains constant, which we replicate by using the bulk quantities.

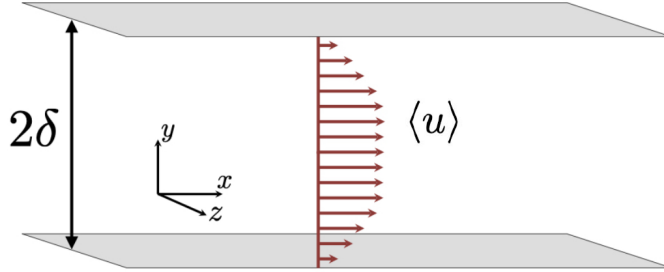


Figure 3-1: Canonical channel flow.

The domain is discretized with different grid resolutions  $\Delta/\delta = 0.2, 0.1$ , and  $0.05$ , corresponding to 10, 20, and 40 points per channel height for the WMLES run with the DSM SGS model and EQWM. Results using the IP SGS model are computed using 24 points per channel height. We tabulate the different flow cases in Table 3.1.

Table 3.1: Channel flow cases for WMLES

Case	M	Re	Points/2 $\delta$	$\Delta/\delta$
1	0.8	17,000	10, 20, 40	0.2, 0.1, 0.05
2	0.8	34,000	10, 20, 40	0.2, 0.1, 0.05
3	1.5	17,000	10, 20, 40	0.2, 0.1, 0.05
4	1.5	17,000	10, 20, 40	0.2, 0.1, 0.05
5	3.0	24,000	10, 20, 40	0.2, 0.1, 0.05
6	3.0	15,000	10, 20, 40	0.2, 0.1, 0.05

### 3.3 Quantities of interest

The performance of the DSM SGS model is assessed by characterizing the error scaling properties of the quantities of interest with Mach number, Reynolds number, and grid resolution. The error in a given quantity of interest  $q$  is assumed to follow

$$\varepsilon_q \sim \left( \frac{\Delta}{\delta} \right)^\alpha \text{Re}^\beta M^\gamma. \quad (3.1)$$

The performance of the IP SGS model is evaluated in the prediction of the mean velocity and temperature profiles and compared against the predictions provided by the DSM SGS model and DNS.

### 3.4 Theoretical estimations

We study theoretically the scaling properties of the mean velocity profile and the mean temperature profile and assess our conclusions experimentally through simulation [32, 66]. We assume that the scaling of the error can be approximated by

$$\varepsilon_q \sim \frac{\langle q_{\text{LES}} \rangle - \langle q_{\text{DNS}} \rangle}{\langle q_{\text{DNS}} \rangle}, \quad (3.2)$$

where the subscripts denote either the LES or DNS solution. We consider the streamwise ( $x$ -direction) momentum equation

$$\frac{\partial \rho u}{\partial t} + \frac{\partial \rho uu_j}{\partial x_j} = -\frac{\partial p}{\partial x} + \frac{1}{\text{Re}} \frac{\partial \sigma_{1j}}{\partial x_j}. \quad (3.3)$$

We multiply by  $u$  and average in the homogeneous directions and time to obtain

$$0 = -\langle u \rangle \frac{\partial \langle \rho uv \rangle}{\partial y} - \langle u \frac{\partial p}{\partial x} \rangle + \frac{1}{\text{Re}} \langle u \rangle \frac{\partial \langle \sigma_{12} \rangle}{\partial y}. \quad (3.4)$$

We can do the same for the filtered streamwise momentum equation from LES

$$\frac{\partial \bar{\rho} \tilde{u}}{\partial t} + \frac{\partial \bar{\rho} \tilde{u} \tilde{u}_j}{\partial x_j} = -\frac{\partial \bar{p}}{\partial x} + \frac{1}{\text{Re}} \frac{\partial \bar{\sigma}_{1j}}{\partial x_j} - \frac{\partial \tau_{1j}}{\partial x_j}. \quad (3.5)$$

Now, we multiply by  $\tilde{u}$  and average in the homogeneous directions and time to obtain

$$0 = -\langle \tilde{u} \rangle \frac{\partial \langle \bar{\rho} \tilde{u} \tilde{v} \rangle}{\partial y} - \langle \tilde{u} \frac{\partial \bar{p}}{\partial x} \rangle + \frac{1}{\text{Re}} \langle \tilde{u} \rangle \frac{\partial \langle \bar{\sigma}_{12} \rangle}{\partial y} - \langle \tilde{u} \rangle \frac{\partial \langle \tau_{12} \rangle}{\partial y}. \quad (3.6)$$

After subtraction and manipulation of the equations, we obtain

$$\left\langle \tilde{u} \frac{\partial \bar{p}}{\partial x} - u \frac{\partial p}{\partial x} \right\rangle = \langle \tilde{u} \rangle \left[ -\frac{\partial \langle \bar{\rho} \tilde{u} \tilde{v} \rangle}{\partial y} + \frac{1}{\text{Re}} \frac{\partial \langle \bar{\sigma}_{ij} \rangle}{\partial y} - \frac{\partial \langle \tau_{12} \rangle}{\partial y} \right] - \langle u \rangle \left[ \frac{1}{\text{Re}} \frac{\partial \langle \sigma_{12} \rangle}{\partial y} - \frac{\partial \langle \rho uv \rangle}{\partial y} \right], \quad (3.7)$$

$$\frac{\langle \tilde{u} \rangle - \langle u \rangle}{\langle u \rangle} = \frac{\left\langle \tilde{u} \frac{\partial \bar{p}}{\partial x} - u \frac{\partial p}{\partial x} \right\rangle - \langle u \rangle}{\langle u \rangle} + \frac{\left[ \frac{1}{\text{Re}} \frac{\partial \langle \sigma_{12} \rangle}{\partial y} - \frac{\partial \langle \rho uv \rangle}{\partial y} \right]}{\left[ -\frac{\partial \langle \bar{\rho} \tilde{u} \tilde{v} \rangle}{\partial y} + \frac{1}{\text{Re}} \frac{\partial \langle \bar{\sigma}_{ij} \rangle}{\partial y} - \frac{\partial \langle \tau_{12} \rangle}{\partial y} \right]}, \quad (3.8)$$

and thus we can look at the right-hand side to give insight into the scaling properties. We can deduce that for higher Reynolds numbers, the pressure difference and compressibility effects will play a greater role in the error in the mean velocity profile.

Thus, we can anticipate that the error in the mean velocity profile will show some dependence with Mach number.

For the mean temperature, we consider the temperature form of the energy equation in the streamwise direction

$$\frac{\partial}{\partial t}(\rho C_v T) + \frac{\partial}{\partial x_j}(\rho u_j C_v T) = -\gamma M^2(\gamma - 1)p \frac{\partial u_j}{\partial x_j} + \frac{\gamma M^2(\gamma - 1)}{Re} \sigma_{1j} \frac{\partial u}{\partial x_j} - \frac{\gamma}{RePr} \frac{\partial Q_j}{\partial x_j}, \quad (3.9)$$

where  $u$  denotes the velocity in the streamwise direction. We multiply by  $T$  for the energy equation and take the average in the homogeneous directions and time to obtain

$$0 = -\langle T \rangle \frac{\partial \langle \rho v C_v T \rangle}{\partial y} - \langle T \rangle \gamma M^2(\gamma - 1) \langle p \rangle \frac{\partial \langle v \rangle}{\partial y} + \langle T \rangle \frac{\gamma M^2(\gamma - 1)}{Re} \langle \sigma_{12} \rangle \frac{\partial \langle u \rangle}{\partial y} - \langle T \rangle \frac{\gamma}{RePr} \frac{\partial \langle Q_2 \rangle}{\partial y}, \quad (3.10)$$

where  $Q_2$  is a component of the heat flux vector. We can do the same for the filtered temperature form of the energy equation from LES

$$\frac{\partial}{\partial t}(\bar{\rho} C_v \tilde{T}) + \frac{\partial}{\partial x_j}(\bar{\rho} \tilde{u}_j C_v \tilde{T}) + \frac{\partial q_1}{\partial x_j} = -\gamma M^2(\gamma - 1) \bar{p} \frac{\partial \tilde{u}_j}{\partial x_j} + \frac{\gamma M^2(\gamma - 1)}{Re} \overline{\sigma_{1j} \frac{\partial u}{\partial x_j}} - \frac{\gamma}{RePr} \frac{\partial \overline{Q_j}}{\partial x_j} \quad (3.11)$$

We multiply by  $\tilde{T}$  and take the average in the homogeneous directions and time to obtain

$$0 = -\langle \tilde{T} \rangle \frac{\partial \langle \bar{\rho} \tilde{v} C_v \tilde{T} \rangle}{\partial y} - \langle \tilde{T} \rangle \frac{\partial \langle q_1 \rangle}{\partial y} - \langle \tilde{T} \rangle \gamma M^2(\gamma - 1) \langle \bar{p} \rangle \frac{\partial \langle \tilde{v} \rangle}{\partial y} + \langle \tilde{T} \rangle \frac{\gamma M^2(\gamma - 1)}{Re} \left\langle \overline{\sigma_{12} \frac{\partial u}{\partial y}} \right\rangle - \langle \tilde{T} \rangle \frac{\gamma}{RePr} \frac{\partial \langle \overline{Q_2} \rangle}{\partial y}, \quad (3.12)$$

where  $q_1$  is a component of the SGS heat flux vector. After subtraction and manipu-

lation of the equations, we obtain

$$0 = \langle \tilde{T} \rangle \left[ -\frac{\partial \langle \bar{\rho} \tilde{v} C_v \tilde{T} \rangle}{\partial y} - \frac{\partial \langle q_1 \rangle}{\partial y} - \gamma M^2 (\gamma - 1) \langle \bar{p} \rangle \frac{\partial \langle \tilde{v} \rangle}{\partial y} + \frac{\gamma M^2 (\gamma - 1)}{\text{Re}} \left\langle \sigma_{12} \frac{\partial u}{\partial y} \right\rangle \right. \\ \left. - \frac{\gamma}{\text{RePr}} \frac{\partial \langle \bar{Q}_2 \rangle}{\partial y} \right] - \langle T \rangle \left[ -\frac{\partial \langle \rho v C_v T \rangle}{\partial y} - \gamma M^2 (\gamma - 1) \langle p \rangle \frac{\partial \langle v \rangle}{\partial y} \right. \\ \left. + \frac{\gamma M^2 (\gamma - 1)}{\text{Re}} \langle \sigma_{12} \rangle \frac{\partial \langle u \rangle}{\partial y} - \frac{\gamma}{\text{RePr}} \frac{\partial \langle Q_2 \rangle}{\partial y} \right], \quad (3.13)$$

$$\frac{\langle \tilde{T} \rangle - \langle T \rangle}{\langle T \rangle} = \\ \frac{-\frac{\partial \langle \rho v C_v T \rangle}{\partial y} - \gamma M^2 (\gamma - 1) \left[ \langle p \rangle \frac{\partial \langle v \rangle}{\partial y} + \frac{\langle \sigma_{12} \rangle}{\text{Re}} \frac{\partial \langle u \rangle}{\partial y} \right] - \frac{\gamma}{\text{RePr}} \frac{\partial \langle Q_2 \rangle}{\partial y}}{-\frac{\partial \langle \bar{\rho} \tilde{v} C_v \tilde{T} \rangle}{\partial y} - \frac{\partial \langle q_1 \rangle}{\partial y} - \gamma M^2 (\gamma - 1) \left[ \langle \bar{p} \rangle \frac{\partial \langle \tilde{v} \rangle}{\partial y} + \frac{1}{\text{Re}} \left\langle \sigma_{12} \frac{\partial u}{\partial y} \right\rangle \right] - \frac{\gamma}{\text{RePr}} \frac{\partial \langle \bar{Q}_2 \rangle}{\partial y}} - 1, \quad (3.14)$$

and thus can come to some conclusions on the scaling properties from this relationship. We see dependence on the Mach number explicitly. Therefore, we can expect to see strong dependence on compressibility effects and some dependence on the Reynolds number.

## 3.5 Numerical results

### 3.5.1 Dynamic Smagorinsky model

#### Mean profiles

We assess the error scaling properties for the mean temperature profile computed using the DSM SGS model given by

$$\varepsilon_T = \left[ \frac{\int_{0.2\delta}^{\delta} (\langle T_{\text{LES}} \rangle - \langle T_{\text{DNS}} \rangle)^2 dy}{\int_{0.2\delta}^{\delta} \langle T_{\text{DNS}} \rangle^2 dy} \right]^{1/2}, \quad (3.15)$$

where the choice of bounds excludes very close to the wall [32]. We first present the mean temperature profiles using the DSM SGS model for the different grid resolutions for both subsonic and supersonic flows compared to DNS data in Figure 3-2a and Figure 3-2b, respectively. The temperature is normalized using the temperature at the wall  $T_w$ .

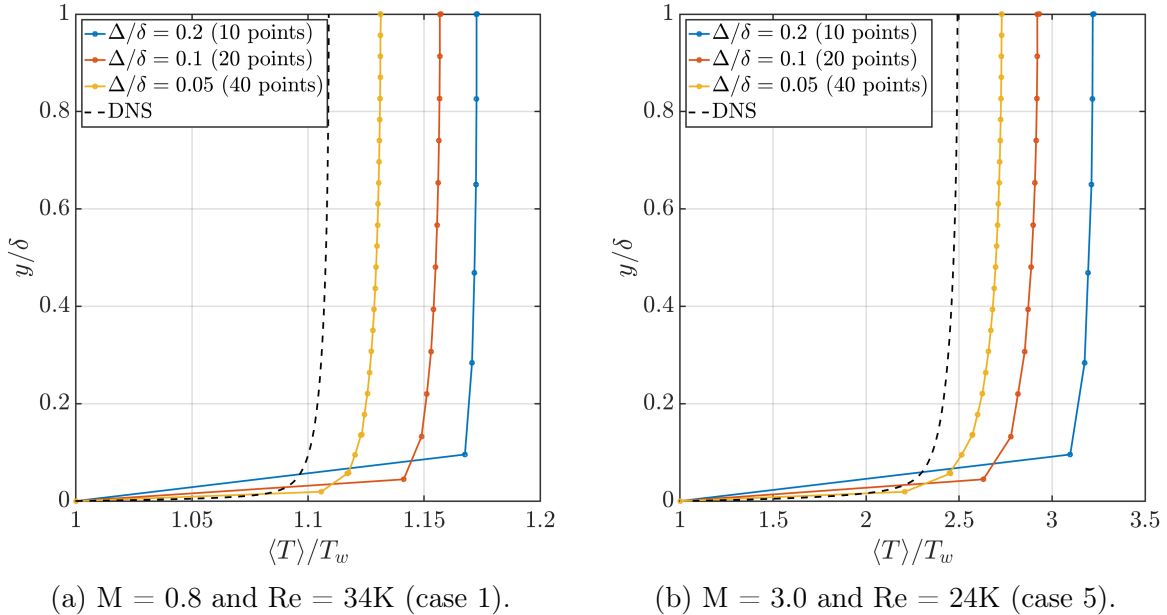


Figure 3-2: Mean temperature profiles.

The mean temperature profile prediction approaches the DNS profile as the grid is refined. Further, the magnitude of the mean temperature values are greater than in the subsonic flow. This result is consistent with insights from the non-dimensional governing equations relating Mach number to temperature showing that higher speed flows will have greater mean temperature values. In general, for both cases, the mean temperature profile is overpredicted by WMLES.

We can quantify the error scaling properties of the mean temperature profile with grid resolution, Reynolds number, and Mach number. Figure 3-3a shows  $\varepsilon_T$  plotted on a log scale with the grid resolution  $\Delta/\delta$  along with a first-order scaling line for reference  $\mathcal{O}(\Delta/\delta)$ . Figure 3-3b shows  $\varepsilon_T$  plotted on a log scale with Reynolds number along with a first-order scaling line for reference  $\mathcal{O}(Re)$ . Figure 3-3c shows  $\varepsilon_T$  plotted on a log scale with Mach number along with a first-order scaling line for reference

$\mathcal{O}(M)$ .

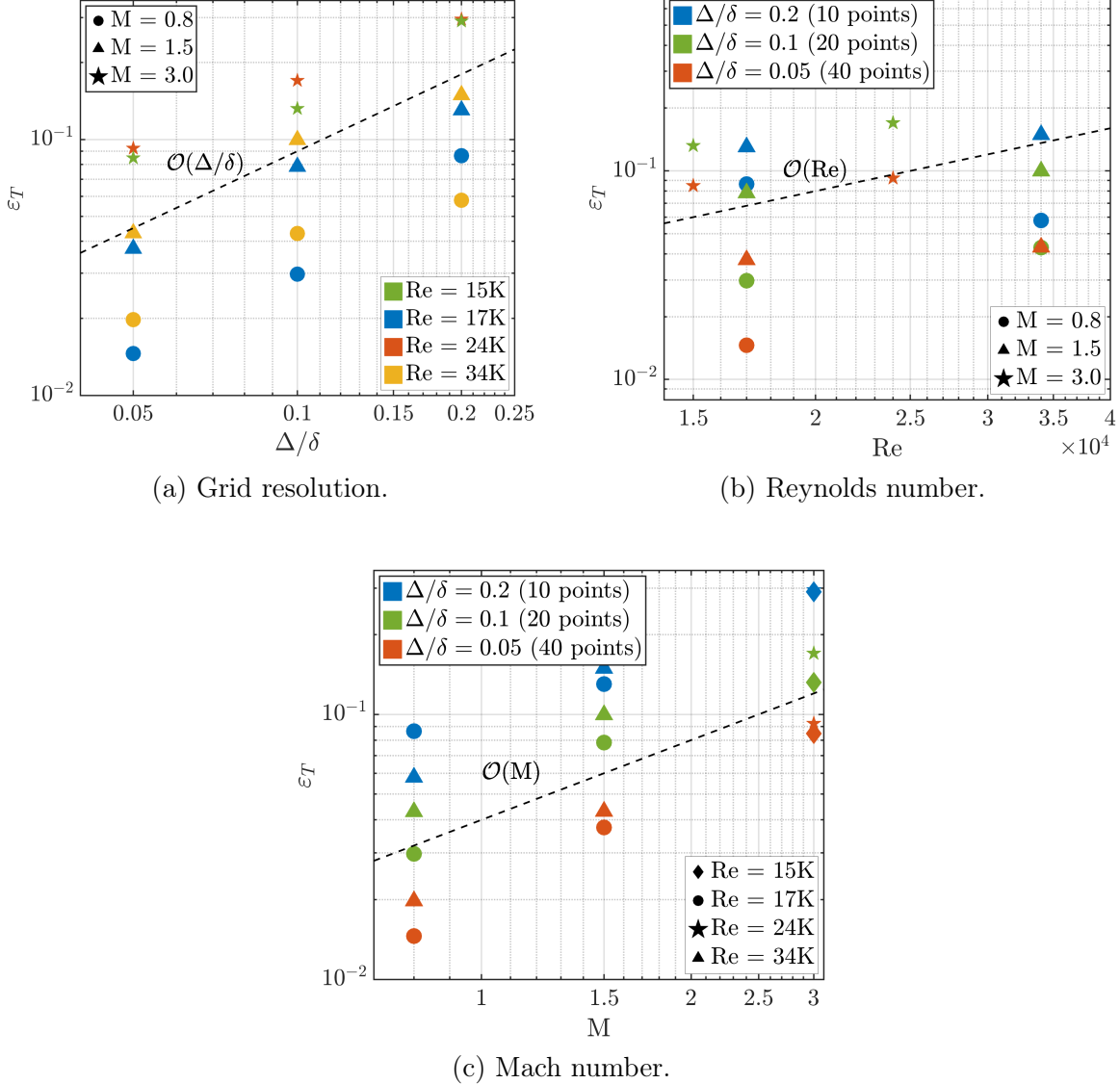


Figure 3-3: Error scaling of mean temperature profile.

To assess error scaling, we assume Eq. 3.15 scales according to the definition presented in Eq. 3.1 as

$$\varepsilon_T \sim \left( \frac{\Delta}{\delta} \right)^\alpha \text{Re}^\beta M^\gamma \quad (3.16)$$

Figure 3-3a shows that the errors approximately scale with  $\mathcal{O}(\Delta/\delta)$ , meaning that  $\alpha \approx 1$  for the mean temperature profile. Looking at Figure 3-3b, we observe different

trends depending on the Mach number of the flow. So, we approximate that for subsonic flow,  $\beta \approx 1/2$ , while for supersonic flow, we do not see any dependence on Reynolds number, and so  $\beta = 0$ . Lastly, Figure 3-3c shows that  $\gamma \approx 1$ . The results for the exponential fittings for grid resolution, Reynolds number, and Mach number are tabulated in Table 3.2.

Table 3.2: Error scaling properties for mean temperature profile

	$M < 1$	$M > 1$
$\alpha$	1	1
$\beta$	$1/2$	0
$\gamma$	1	1

We can use a contour scatter plot to visualize the magnitude of the error in the mean temperature profile prediction with Mach number and Reynolds number for all of the flow cases. Figure 3-4 shows the percent error of  $\varepsilon_T$  plotted relative to all of the flow cases.

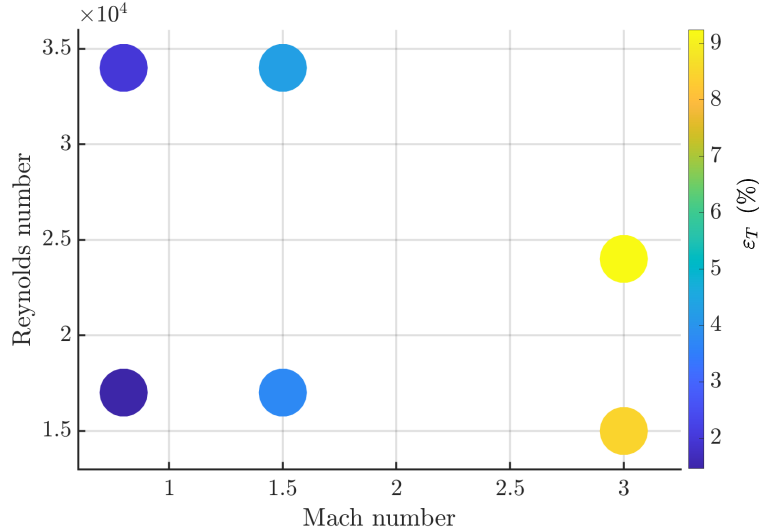


Figure 3-4: Percent error of mean temperature profile for all flow cases.

It is clear from the scatter plot that the magnitude of the error in the mean temperature profile prediction increases as Mach number increases, indicating that the

prediction given by WMLES becomes increasingly worse for higher speed flows. Further, we do not see significant difference in the magnitude of the error with Reynolds number while keeping the Mach number constant. In other words, the prediction of the mean temperature profile is less dependent on Reynolds number than on Mach number.

Characterizing the error scaling properties for the mean velocity profile follows similarly

$$\varepsilon_u = \left[ \frac{\int_{0.2\delta}^{\delta} (\langle u_{\text{LES}} \rangle - \langle u_{\text{DNS}} \rangle)^2 dy}{\int_{0.2\delta}^{\delta} \langle u_{\text{DNS}} \rangle^2 dy} \right]^{1/2}. \quad (3.17)$$

We first present the mean velocity profiles using the DSM SGS model for the different grid resolutions for both subsonic and supersonic flows compared to DNS data in Figure 3-5a and Figure 3-5b, respectively. The velocity is normalized using the centerline velocity value  $u_c$ .

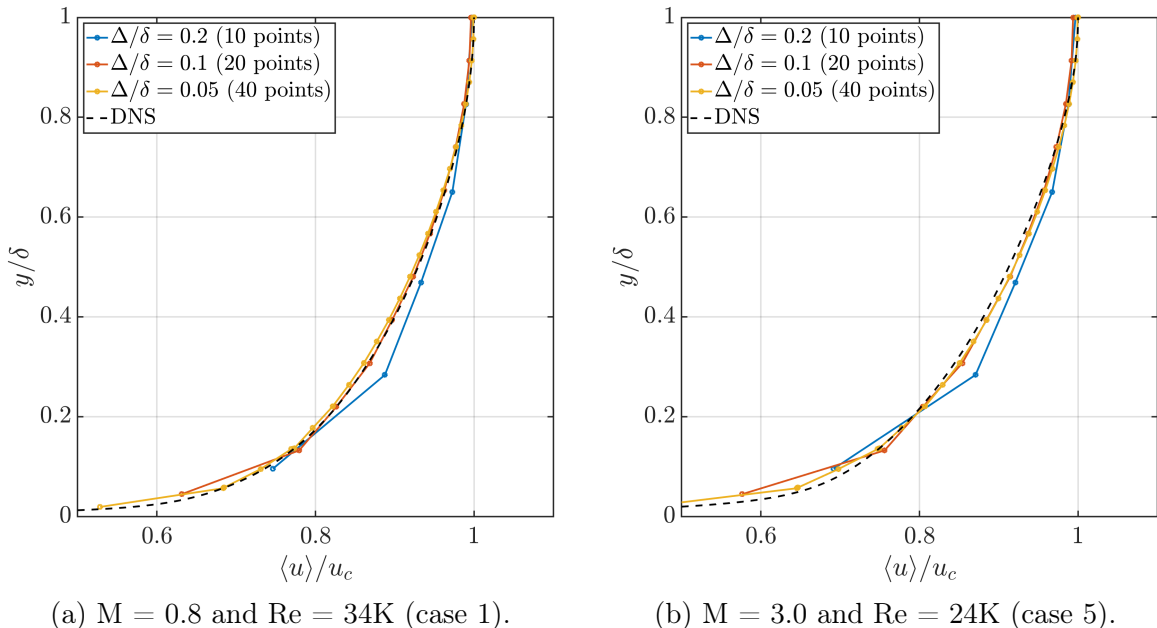


Figure 3-5: Mean velocity profiles.

The mean velocity profile is fairly well predicted even with the coarsest grid resolution used. We can quantify the error scaling properties of the mean velocity profile with grid resolution and Mach number. Figure 3-6a shows  $\varepsilon_u$  plotted on a log scale

with the grid resolution  $\Delta/\delta$  along with a first-order scaling line for reference  $\mathcal{O}(\Delta/\delta)$ . Figure 3-6b shows  $\varepsilon_u$  plotted on a log scale with Mach number along with a first-order scaling line for reference  $\mathcal{O}(M)$ .

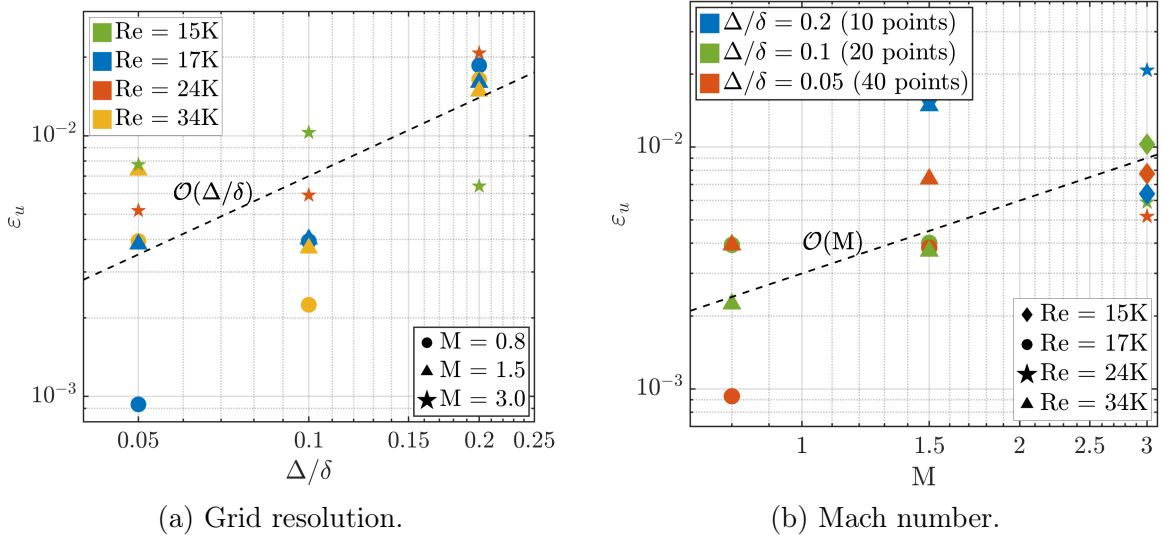


Figure 3-6: Error scaling of mean velocity profile.

To assess error scaling, we assume again that Eq. 3.17 scales according to the definition presented in Eq. 3.1 as

$$\varepsilon_u \sim \left( \frac{\Delta}{\delta} \right)^\alpha \text{Re}^\beta M^\gamma \quad (3.18)$$

Figure 3-6a shows that the errors scale differently depending on the Mach number of the flow. We estimate that  $\alpha \approx 2$  for subsonic flow, while  $\alpha \approx 0$  for supersonic flow, meaning that there is less dependence on the grid resolution for higher speed flows. From Figure 3-6b, we conclude  $\gamma \approx 1$ . The results for the exponential fittings for grid resolution, Reynolds number, and Mach number are tabulated in Table 3.3.

Table 3.3: Error scaling properties for mean velocity profile

	$M < 1$	$M > 1$
$\alpha$	2	0
$\beta$	2	0
$\gamma$	1	1

We can use a contour scatter plot to visualize the magnitude of the error in the mean velocity profile prediction with Mach number and Reynolds number for all of the flow cases. Figure 3-7 shows the percent error of  $\varepsilon_u$  plotted relative to all of the flow cases.

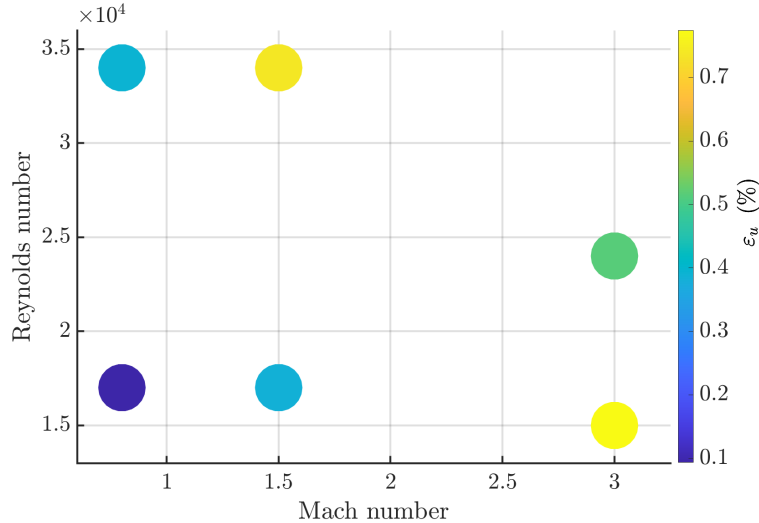


Figure 3-7: Percent error of mean velocity profile for all flow cases.

We first notice the low magnitude of the errors overall at less than 1% for all cases tested. However, we can still draw some conclusions from these results. We see that for lower Mach numbers, there seems to be more dependence on the Reynolds number. The prediction of the mean velocity profile is less accurate for higher Reynolds number for flows at the same Mach number for low speeds. We do not see that trend hold for the higher Mach number case, again emphasizing that Reynolds number has less importance for higher speed flows. This conclusion again highlights the significance

of compressibility effects characterized by higher Mach number.

## Wall quantities

We are interested in assessing the prediction for the heat flux at the wall defined by

$$B_q = -\frac{(\gamma - 1)M^2}{u_b/u_\tau} \quad (3.19)$$

which has a direct relationship with the bulk Mach number [58]. So, we also expect to see a relationship with temperature. In this definition,  $u_\tau$  is the WMLES friction velocity, such that the denominator is in wall units.

We determine empirical estimations for the exponents for the error expression for heat flux at the wall

$$\varepsilon_{B_q} \sim \left( \frac{\Delta}{\delta} \right)^\alpha Re^\beta M^\gamma. \quad (3.20)$$

We first present the heat flux at the wall predictions with Mach number using the DSM SGS model for the different flow cases compared to DNS data in Figure 3-8. Each symbol has a corresponding black symbol representing the DNS result.

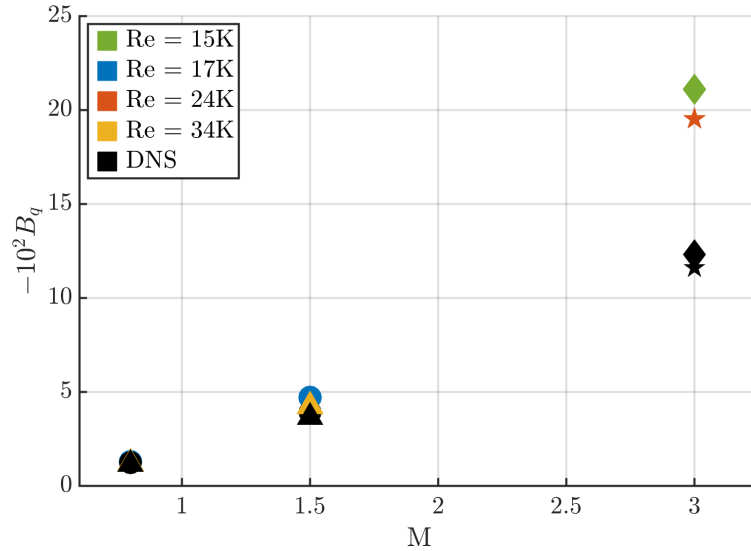


Figure 3-8: Heat flux at the wall with Mach number.

Figure 3-9 shows  $\varepsilon_{B_q}$  plotted on a log scale with the Mach number along with a

second-order scaling line for reference  $\mathcal{O}(M^2)$ .

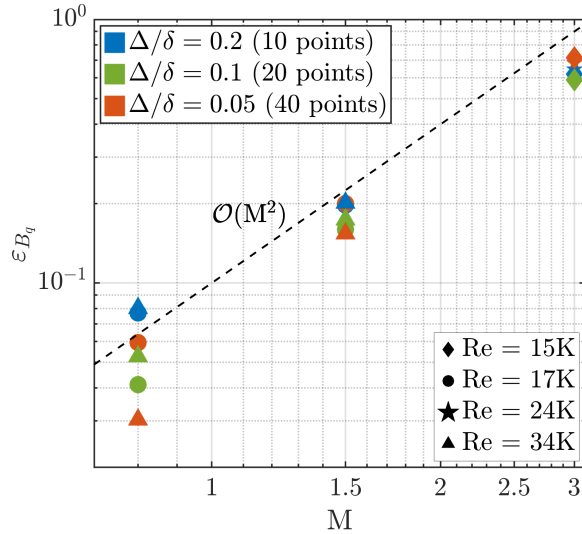


Figure 3-9: Error scaling of heat flux at the wall with Mach number.

From Figure 3-9, we can estimate that  $\gamma \approx 2$ , which is consistent with the heat flux having a direct relationship with the Mach number. We tabulate the results for the exponential fittings for grid resolution, Reynolds number, and Mach number in Table 3.4.

Table 3.4: Error scaling properties for heat flux at the wall

	$M < 1$	$M > 1$
$\alpha$	1	0
$\beta$	0	0
$\gamma$	2	2

We can use a contour scatter plot to visualize the magnitude of the error in the heat flux at the wall prediction with Mach number and Reynolds number for all of the flow cases. Figure 3-10 shows the percent error of  $\varepsilon_{B_q}$  plotted relative to all of the flow cases.

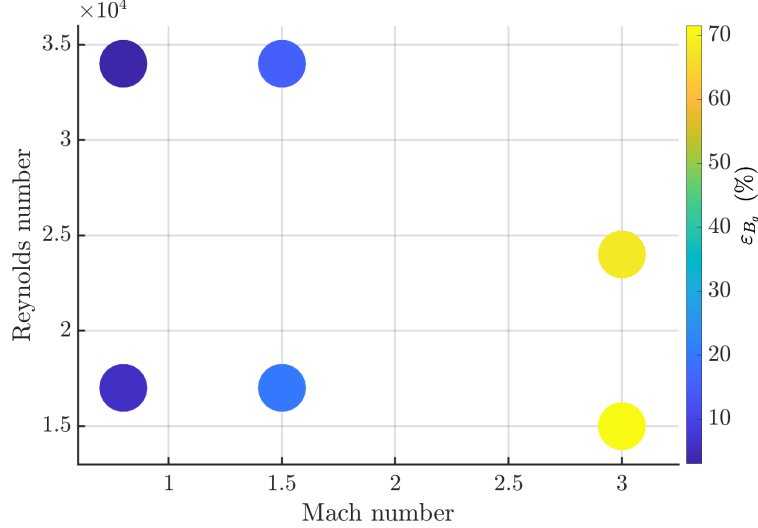


Figure 3-10: Percent error of heat flux at the wall for all flow cases.

Similar to the trends in the error for the mean temperature profile, the magnitude of the error in the heat flux prediction increases as Mach number increases, indicating that the prediction given by WMLES becomes increasingly worse for higher speed flows. Further, we do not see significant difference in the magnitude of the error as we change the Reynolds number while keeping the Mach number the same for the flow. In other words, the prediction of the heat flux at the wall is less dependent on Reynolds number than on Mach number. These results demonstrate the strong coupling between Mach number, temperature, and heat flux. This again emphasizes the enhanced effects of compressibility on temperature and heat flux.

Lastly, we are interested in the accuracy in the prediction of the skin friction coefficient defined by

$$C_f = \frac{2\tau_w}{\rho_b u_b^2}. \quad (3.21)$$

Previous studies have shown that the inner layer of the mean velocity profile is a direct consequence of the variation and balance between the viscous and turbulent shear stresses, so a direct relationship with velocity is expected [58]. We further expect to see some dependence on the Reynolds number for similar reasons.

We determine empirical estimations for the exponents for the error expression for

skin friction coefficient

$$\varepsilon_{C_f} \sim \left( \frac{\Delta}{\delta} \right)^\alpha \text{Re}^\beta M^\gamma. \quad (3.22)$$

We first present the skin friction coefficient predictions with Mach number using the DSM SGS model for the different flow cases compared to DNS data in Figure 3-11.

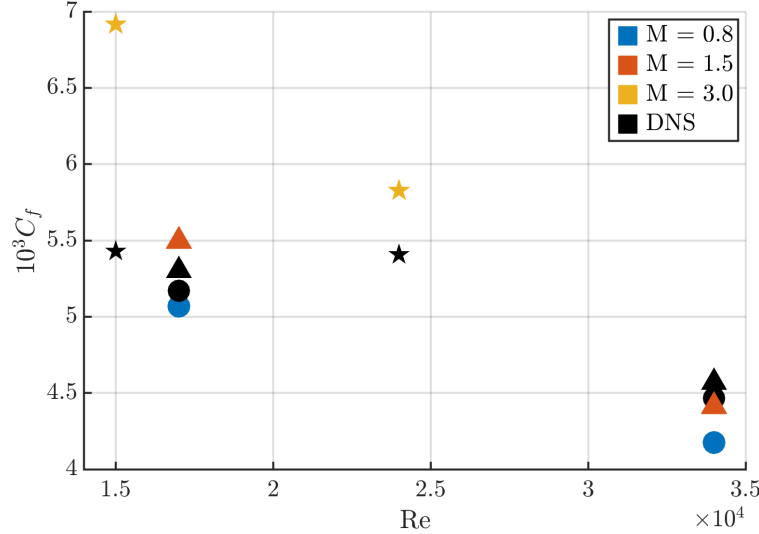


Figure 3-11: Skin friction coefficient with Mach number.

We quantify the error scaling properties of the skin friction coefficient with Reynolds number and Mach number. Figure 3-12a shows  $\varepsilon_{C_f}$  plotted on a log scale with the Reynolds number along with a first-order scaling line for reference  $\mathcal{O}(\text{Re})$ . Figure 3-12b shows  $\varepsilon_{C_f}$  plotted on a log scale with the Mach number along with a first-order scaling line for reference  $\mathcal{O}(M)$ .

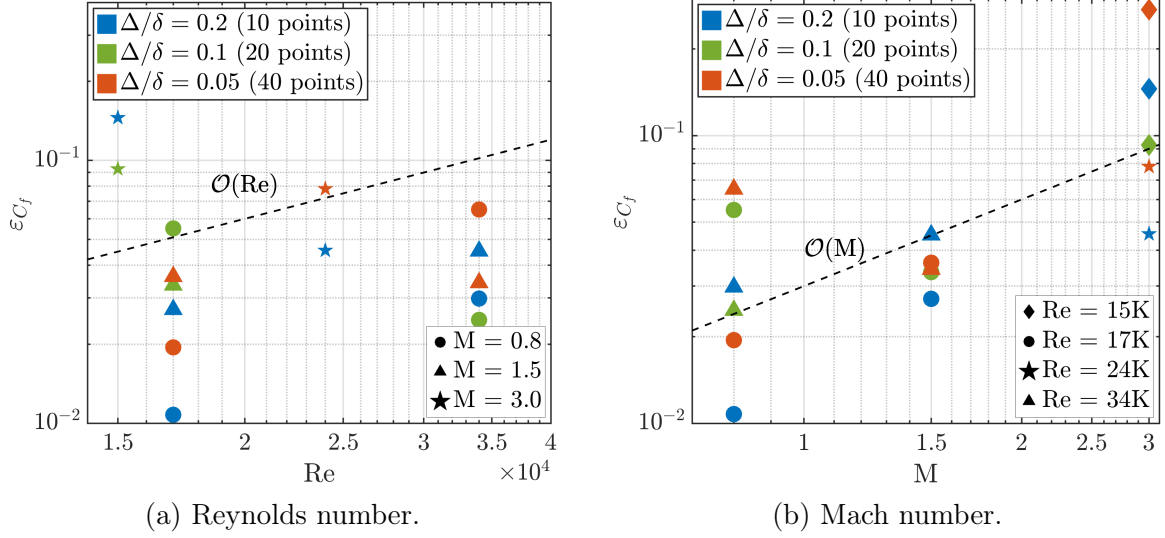


Figure 3-12: Error scaling of mean velocity profile.

From Figure 3-12a, we see that the errors scale differently depending on the Mach number of the flow. We estimate that  $\beta \approx 2$  for subsonic flow, while  $\beta \approx 0$  for supersonic flow. This estimation shows that there is less dependence on the Reynolds number for higher speed flows. Error with the Mach number is shown in Figure 3-12b. It can be estimated that  $\gamma \approx 1$ . We tabulate the results for the exponential fittings for grid resolution, Reynolds number, and Mach number in Table 3.5.

Table 3.5: Error scaling properties for skin friction coefficient

	$M < 1$	$M > 1$
$\alpha$	0	0
$\beta$	2	0
$\gamma$	1	1

We use a contour scatter plot to visualize the magnitude of the error in the skin friction coefficient prediction with Mach number and Reynolds number for all of the flow cases. Figure 3-13 shows the percent error of  $\varepsilon_{C_f}$  plotted relative to all of the flow cases.

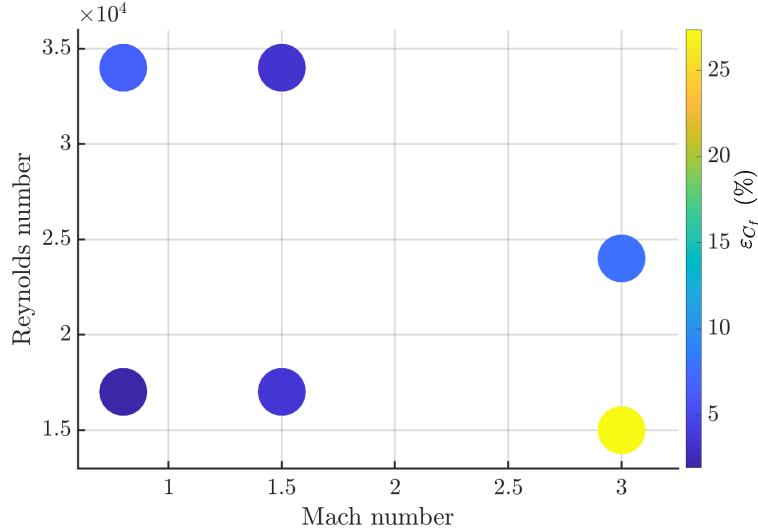


Figure 3-13: Percent error of skin friction coefficient for all flow cases.

We see less visibly noticeable trends of the error in the skin friction coefficient prediction with varying Mach and Reynolds number. However, we can say again that Reynolds number has less of an effect overall, and that errors overall are greater for higher Mach number. We also know that, because of the coupling between skin friction and velocity, some dependence on Reynolds number is expected for this wall quantity, and this dependence is demonstrated here.

## Conclusions

We conclude that mean quantities of interest have the lowest overall errors with  $\varepsilon_T \approx \mathcal{O}(10\%)$  and  $\varepsilon_u \approx \mathcal{O}(1\%)$ . We see low overall errors for the mean velocity profile and less dependence on grid resolution, while the mean temperature profile approaches the DNS data as we refine the grid more. Wall quantities show the highest errors with  $\varepsilon_{B_q} \leq 70\%$  and  $\varepsilon_{C_f} \leq 30\%$ . Further, we see that  $\gamma \geq 1$  for all quantities of interest assessed here. This result is significant for high-speed flows that are compressible and dependent on Mach number. We also see less dependence on Reynolds number for higher speed flows, demonstrated by empirical estimates for  $\beta$ , which agrees with previous studies. We see more dependence on Reynolds number for the skin friction coefficient, and more dependence on Mach number for the heat flux at the wall. We can employ the IP SGS model to improve the mean profile predictions

of the statistical quantities of interest. Table 3.6 consolidates the empirical estimates for all quantities of interest.

Table 3.6: Error scaling properties for quantities of interest

	M < 1			M > 1		
	$\alpha$	$\beta$	$\gamma$	$\alpha$	$\beta$	$\gamma$
$T$	1	$1/2$	1	1	0	1
$u$	2	2	1	0	0	1
$B_q$	1	0	2	0	0	2
$C_f$	0	2	1	0	0	1

### 3.5.2 Information-preserving model

The IP SGS model is now applied to the compressible channel. The mean velocity and temperature profiles predicted by the WMLES for  $M = 3.0$  and  $Re = 24K$  with the IP SGS model are given in Fig. 3-14a and Fig. 3-14b, respectively. DNS data is plotted as a black dashed line for a reference. The profiles are predicted using an EQWM and either IP or DSM SGS model.

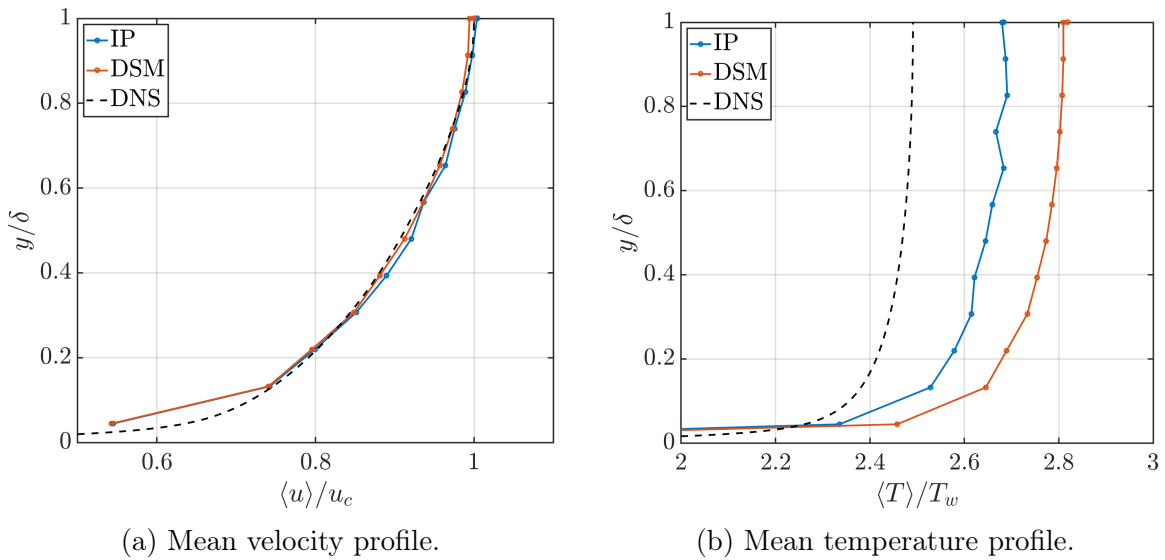


Figure 3-14: Mean profile predictions from IP and DSM SGS models.

The results show that the IP SGS model offers an accuracy comparable to the DSM SGS model in the prediction of the mean velocity profile. This is acceptable since the prediction of the mean velocity profile already is generally accurate. For the mean temperature profile, the prediction given by the IP SGS model is improved compared with the DSM SGS model. Table 3.7 shows the percent error in the prediction of the mean velocity and temperature profiles as calculated using Eq. 3.1. Indeed, it is found that the IP and DSM SGS models both yield predictions of the mean velocity profile within 1% of DNS data. Further, there is 5% improvement in accuracy in the prediction of the temperature profile using the IP SGS model compared to the DSM SGS model.

Table 3.7: Percent error in mean velocity and temperature profiles

	DSM	IP
$\varepsilon_u$	0.4%	0.8%
$\varepsilon_T$	12.4%	7.3%

## 3.6 Conclusions

The information-theoretic formulation presented in this work is shown to be an effective framework for reduced-order modeling of highly chaotic systems with a large number of degrees of freedom. In the case of LES, an SGS model was developed based on minimizing the KL divergence between the probabilities of the model state and the true state, enabling the accurate prediction of the statistical quantities of interest. The model aims at minimizing the information lost between the probability mass distribution of the interscale energy transfer and viscous dissipation at different scales. We have shown that the IP SGS model offers comparable accuracy as the DSM SGS model in the prediction of the mean velocity profile given by DNS data. We have also shown that the IP SGS model yields an improved prediction of the mean temperature profile given by DNS data compared to the DSM SGS model.

# Chapter 4

## External aerodynamic application: X-59 QueSST

### 4.1 Objectives

WMLES of the experimental aircraft X-59 Quiet SuperSonic Technology (QueSST) developed by Lockheed Martin at Skunk Works for NASA's Low-Boom Flight Demonstrator project is conducted using the solver charLES. The primary goal of NASA's Low-Boom Flight Demonstrator project is to demonstrate feasibility of supersonic over-land flight at reduced loudness levels. The X-59 QueSST is being designed and built with technology that reduces the loudness of a sonic boom to a gentle thump to people on the ground. Then, the aircraft will fly over select US communities to gather data on human responses to the sound generated during supersonic flight. New sound-based rules regarding supersonic flight over land will be written and adopted based on this mission, which would enable new commercial cargo and passenger markets to provide faster-than-sound air travel [40].

Near-field CFD is a part of the sonic boom community goal to predict the acoustic signature on the ground and how it is perceived by people. The sonic boom prediction process is shown in Figure 4-1 as provided by the AIAA Sonic Boom Prediction Workshop [40]. The goal is therefore to propagate the near-field pressure signatures to the ground and reduce the properties of these signatures to loudness.

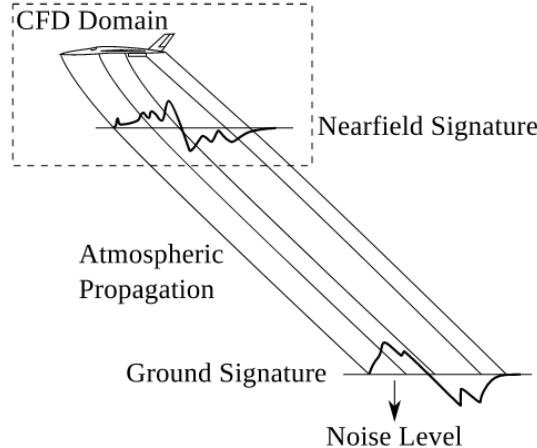


Figure 4-1: Sonic boom prediction process [40].

The capabilities of WMLES to predict the noise level in cruise conditions are evaluated and compared with other numerical studies. This approach will enable the detection of design deficiencies prior to aircraft construction, resulting in financial benefits and accelerating certification by analysis efforts.

Based on results from the previous chapter, we can make initial estimates informed by the error scaling analysis for a grid resolution of  $\Delta/\delta = 0.1$  for the X-59 QueSST at cruise conditions  $M \approx 1.4$  and  $Re \approx \mathcal{O}(10^7)$ . The extrapolated estimates for the errors in the previous quantities of interest are shown in Table 4.1. These estimates show that current models are not expected to do very well in capturing certain quantities of interest. In particular, the models are estimated to struggle in predicting wall quantities of interest. In this chapter, we will assess how well the models can capture shock waves generated by changes in pressure.

Table 4.1: X-59 QueSST error estimates

$q$	$T$	$u$	$B_q$	$C_f$
$\varepsilon_q$	9%	1%	11%	8%

The main quantities of interest are the near-field pressure field and the intensities and locations of the shock waves. We also assess error and convergence properties

compared to previous studies from the AIAA Sonic Boom Prediction Workshop focused on the X-59 QueSST. The workshop included near-field signatures from CFD simulations using various RANS solvers that were then propagated to the ground to compute noise levels. Specifically, we compare pressure signatures at one-body length away from the aircraft to RANS results from Kirz (2022) [24] computed with a grid resolution of 5.74 in/cell. The near-field CFD simulations from Kirz (2022) were performed with the German Aerospace Center (DLR) TAU code, which is based on an unstructured finite-volume approach for solving the RANS equations on hybrid grids [51, 24]. An improved second-order accurate advection upstream splitting method (AUSM) upwind scheme was applied for the spatial discretization of the convective fluxes, and an implicit lower upper symmetric Gauss Seidel scheme is used for time stepping. The AUSMDV scheme is a flux splitting scheme with an aim at removing numerical dissipation on a contact discontinuity for accurate and robust resolution for shocks [63]. The gradients were computed using a Green Gauss approach. The simulations did not include multigrid acceleration. The Spalart-Allmaras (SA)-negative turbulence model was used. Throughout this chapter, we assume that the RANS results are the “truth” when making comparisons. The validity of this assumption is discussed after the presentation of the numerical results and convergence studies.

## 4.2 Physical and computational setup

The simulation is performed using the C608 Low-Boom Flight Demonstrator geometry provided by the AIAA Sonic Boom Prediction workshop shown in Figure 4-2. This geometry configuration is an early iteration of the X-59 final design and is desirable for comparing against RANS results using the same setup. Simulations are performed at cruise conditions at Mach number  $M = 1.4$  and Reynolds number per inch of  $Re/in = 109,776$ . Freestream and boundary conditions are specified in Table 4.2. The C608 has propulsion and environmental control system (ECS) boundary conditions shown in Figure 4-3. The engine bypass exhaust is a semicircular region between the nozzle and aft deck, and the ECS inlet is located in the wing root [40].



Figure 4-2: C608 configuration [40].

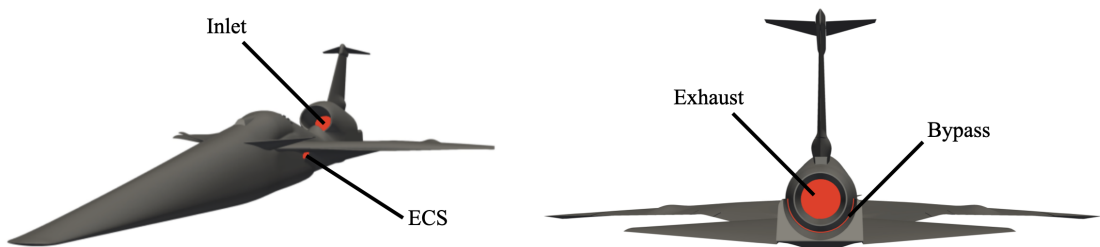


Figure 4-3: C608 boundary conditions.

Table 4.2: C608 freestream and boundary conditions

Description	Condition
Freestream Mach number	1.4
Freestream temperature ( $^{\circ}$ R)	389.9
Altitude (ft)	53,200
Unit Reynolds number (per inch)	109,776
Ratio of engine nozzle plenum total pressure to freestream static pressure	10.0
Ratio of engine nozzle plenum total temperature to freestream static temperature	7.0
Ratio of engine bypass exhaust total pressure to freestream static pressure	2.4
Ratio of engine bypass exhaust total temperature to freestream static temperature	2.0
Ratio of engine fan face static pressure to freestream	2.6
Ratio of ECS inlet static pressure to freestream	1.4

The size of the computational domain is  $2.7L_{BODY} \times 2.7L_{BODY} \times 5.4L_{BODY}$  in the streamwise, wall-normal, and spanwise directions, respectively. Figure 4-4 shows a schematic for computational domain, where the red line denotes the pressure probe placed at one-body length below directly under the aircraft.

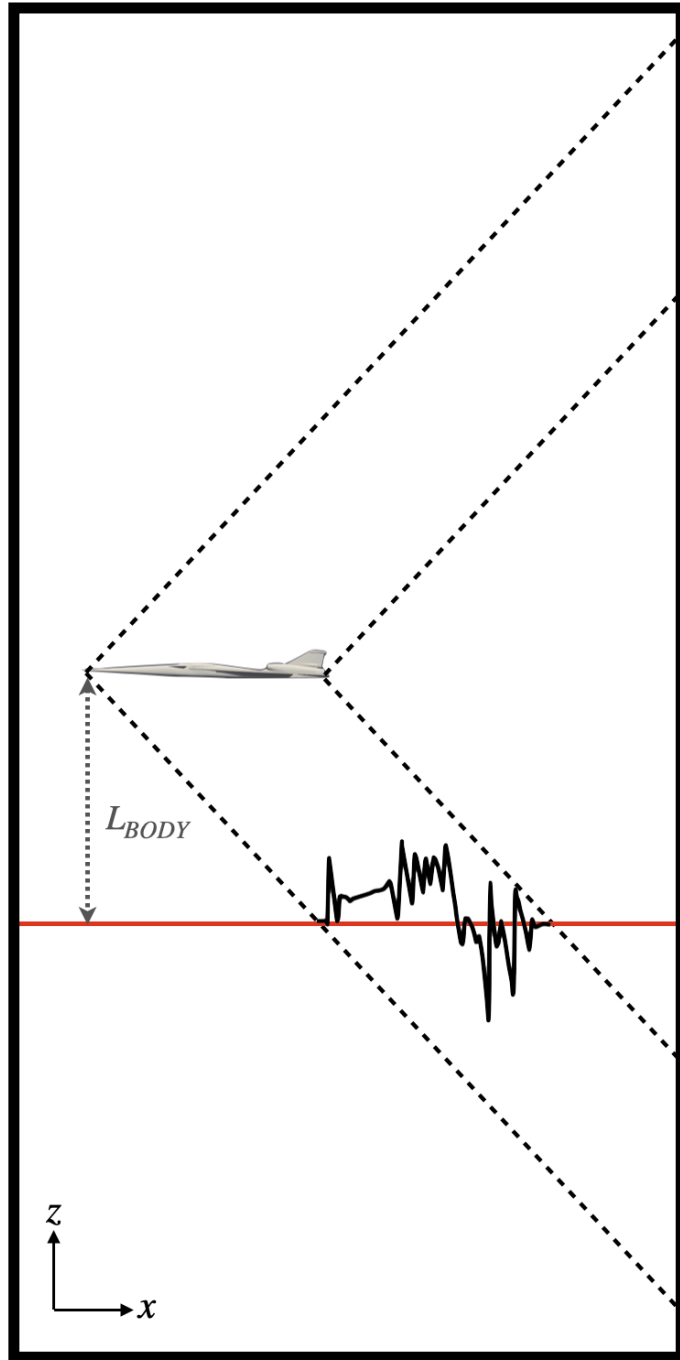


Figure 4-4: Computational domain for X-59 simulations.

The domain is discretized using a cone configuration with additional grid refinement in the plane where the pressure signatures are probed for one half of the symmetric configuration. Figure 4-6a shows the domain discretization in a slice of the  $x$ - $z$  plane, a side view of the aircraft as in Figure 4-4. Figure 4-6b shows a view

of the domain from the front of the aircraft at a slice halfway through the domain. The front and side views show the refinement configuration with a red line to denote the pressure probe. Figure 4-6c shows a top view of the domain discretization. All discretization configurations include enhanced refinement around the body of the aircraft geometry. This refinement was done in Gmsh [18] shown in Figure 4-5.

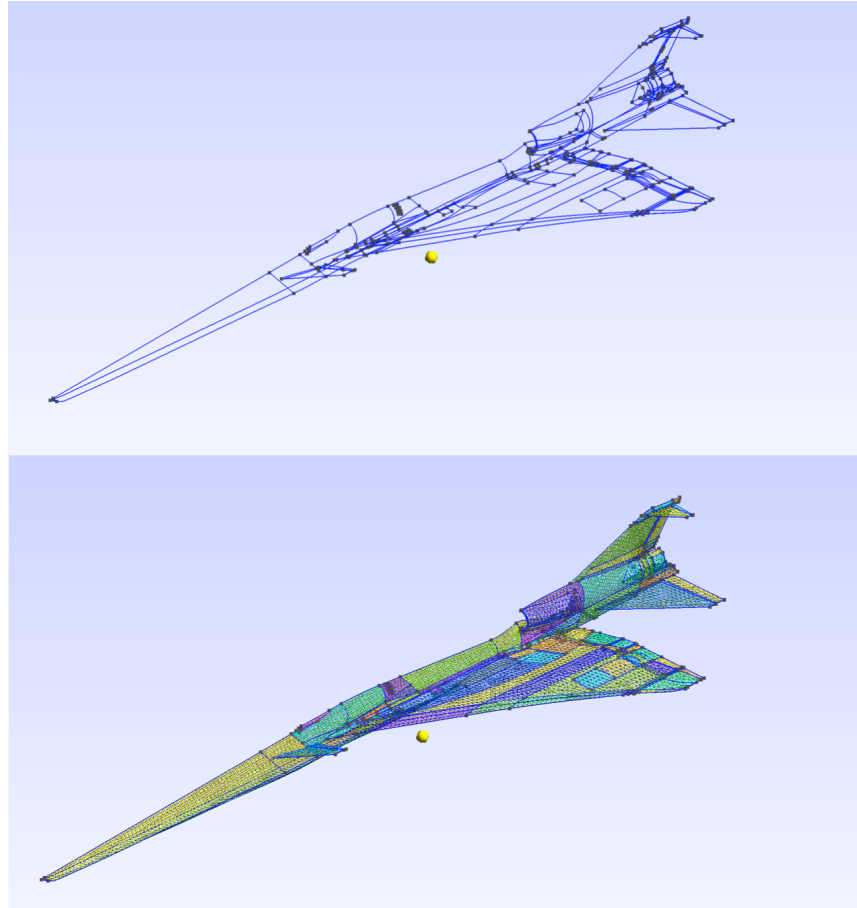
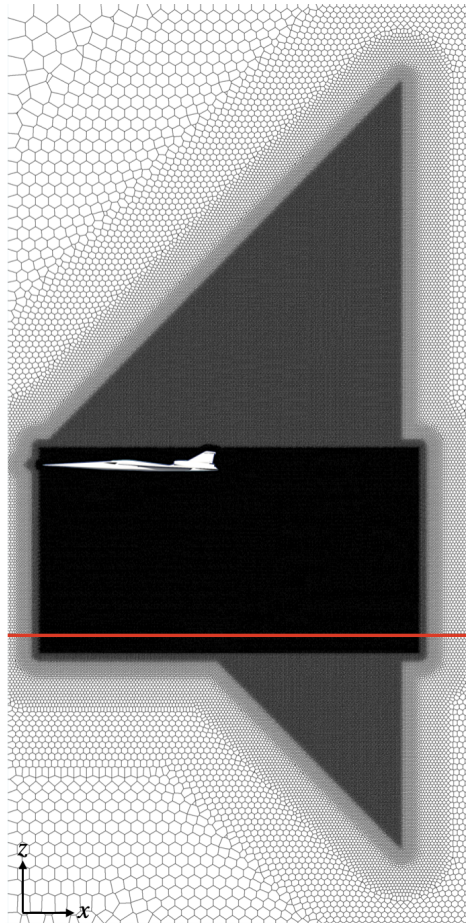
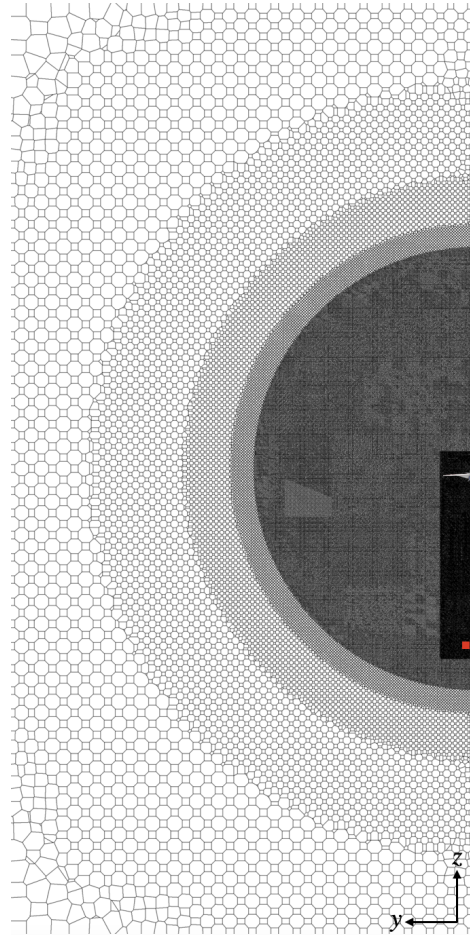


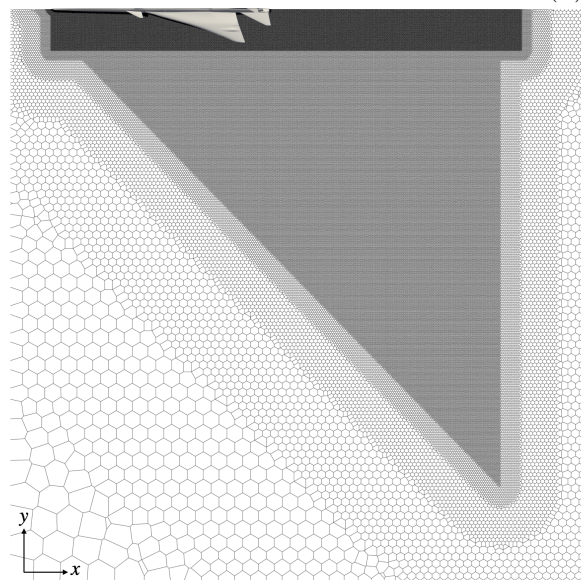
Figure 4-5: Aircraft surface geometry and refinement in Gmsh.



(a) From side.



(b) From front.



(c) From top.

Figure 4-6: Domain discretization views.

The grid resolution of the Mach-aligned cone is coarser than the refinement of the probe-containing plane to preserve the effects of the geometry throughout the domain in shock-containing regions. The grid resolution of the plane is fine enough to capture higher-order oscillations of the pressure signature. Table 4.3 tabulates the different simulation parameters for the X-59 cases run with WMLES. Note that we run cases with both dynamic Smagorinsky and Vreman SGS models.

Table 4.3: X-59 flow cases for WMLES

Case	Cone		Plane		SGS model
	in/cell	Points/ $L_{BODY}$	in/cell	Points/ $L_{BODY}$	
1	20	54	10	108	DSM
2	10	108	5	216	DSM
3	5	216	2.5	432	DSM
4	20	54	10	108	Vreman
5	10	108	5	216	Vreman
6	5	216	2.5	432	Vreman

## 4.3 Numerical results

### 4.3.1 Shock waves

We first present the results for the locations and intensities of the shock waves from both the side and top views in Figure 4-7 and Figure 4-8, respectively. We label shocks produced by the geometry of the aircraft and the boundary conditions imposed, and these qualitative results show good agreement with previous numerical studies. We also show the computational flow visualizations of the side and top views in Figure 4-9 and Figure 4-10, respectively. These visualizations are generated in Paraview to capture the contours in the pressure quantity of interest  $p$  defined by as the percent

difference deviation from the freestream pressure

$$p = \frac{\Delta p}{p_\infty} \times 100, \quad (4.1)$$

where  $\Delta p = p_s - p_\infty$  where  $p_s$  is the pressure measured by the probe and

$$p_\infty = \frac{\rho_\infty}{\gamma} \left( \frac{U_\infty}{M} \right)^2. \quad (4.2)$$

where the subscript  $\infty$  denotes a freestream quantity,  $\gamma = 1.4$ , and  $M = 1.4$ . The pressure visualizations show the surface pressure distribution on the aircraft, also quantified using  $p$  above. The nose creates a shock and expansion pair, followed by a smooth compression. There is a rapid succession of shocks and expansions generated by the wing leading edge, vortex generators, and ECS inlet. The wing trailing edge, horizontal stabilizer, aft deck, tail, plume, and vortices result in more rapid shocks and expansions and other complex interactions [40]. From the surface pressure distribution, we see that inlet spillage creates an area of high pressure over the wing. These results are consistent with those reported through the AIAA Sonic Boom Prediction Workshop [40].

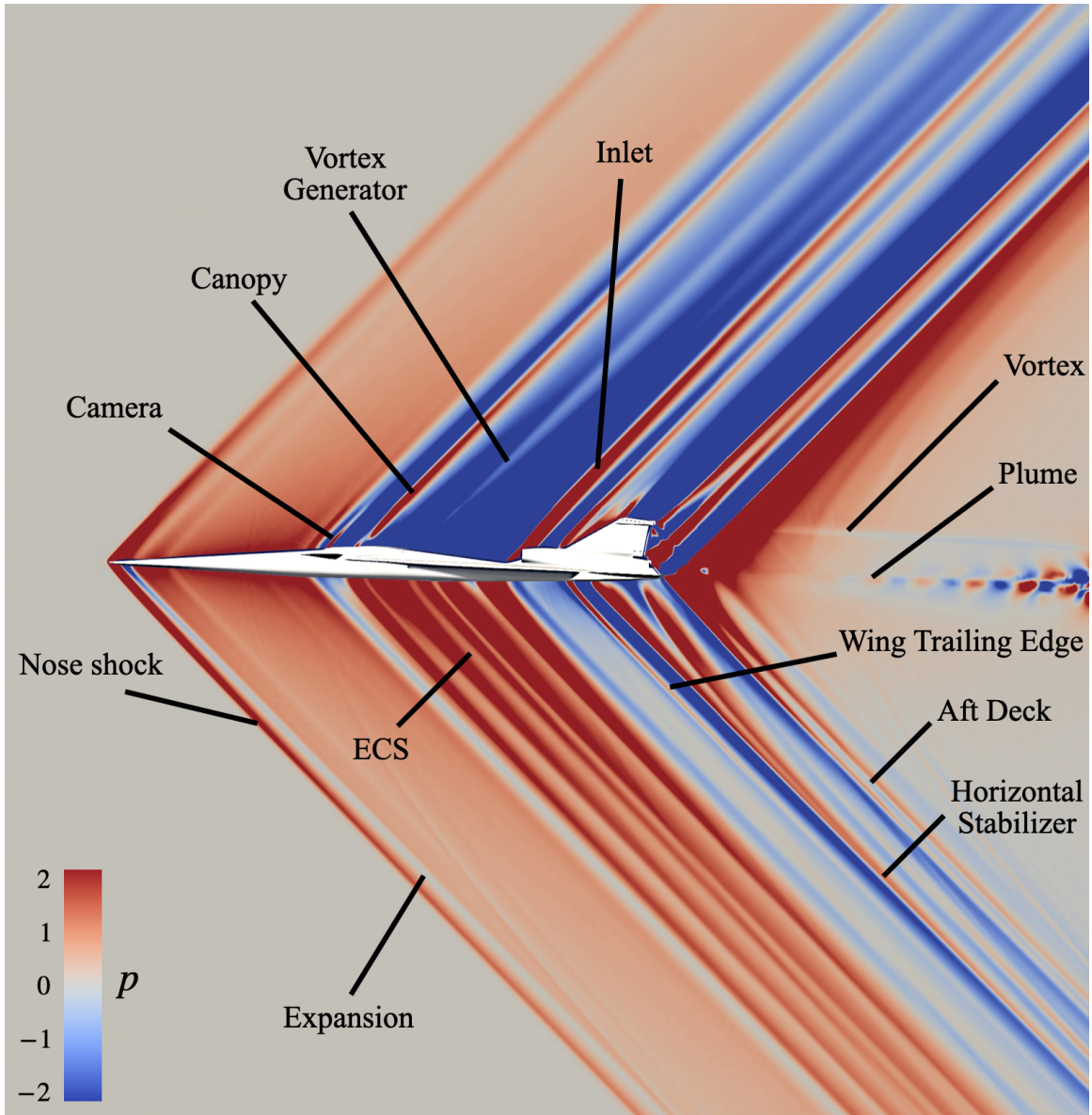


Figure 4-7: Pressure contour visualization from  $x$ - $z$  plane.

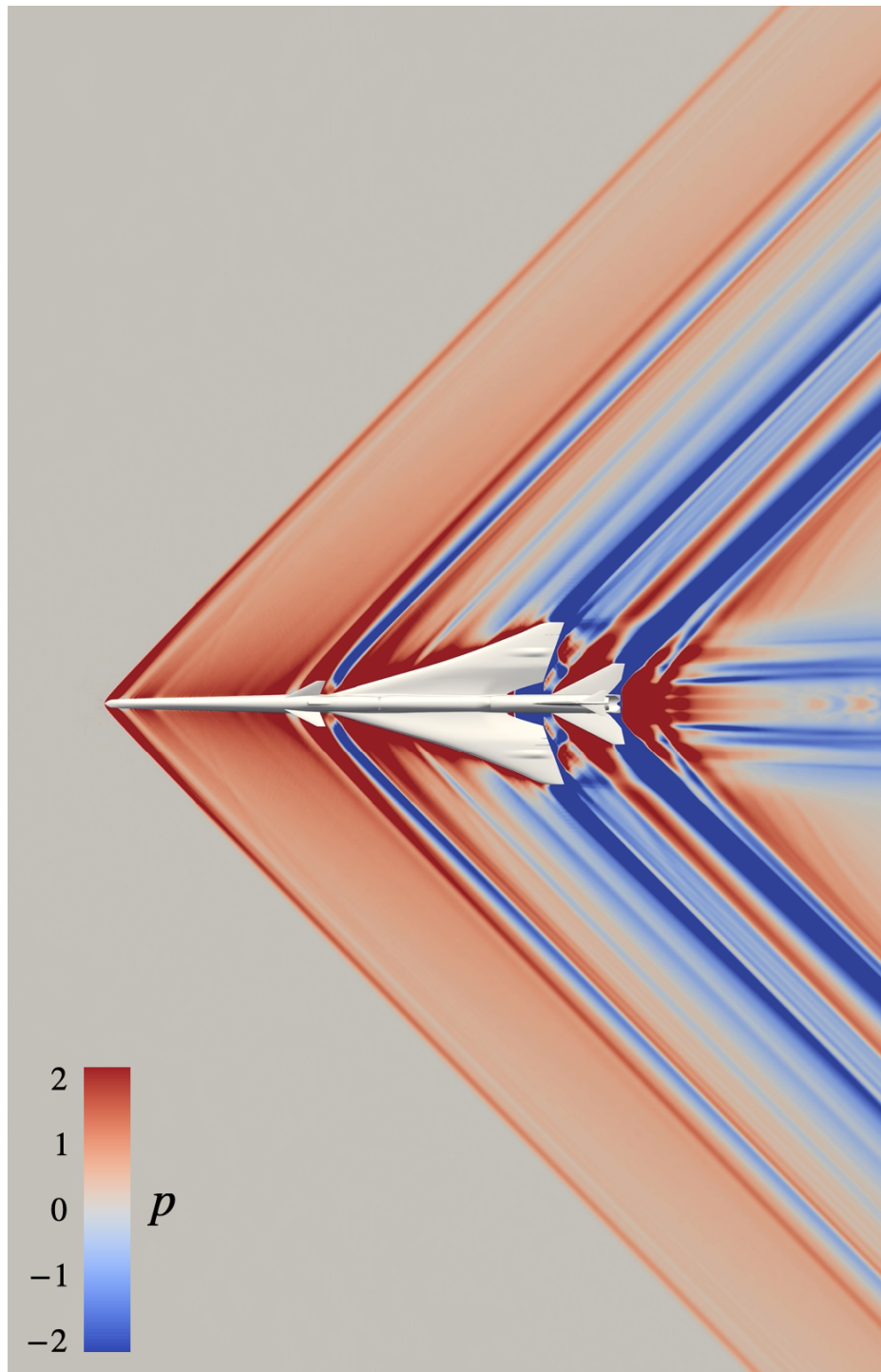


Figure 4-8: Pressure contour visualization from  $x$ - $y$  plane.

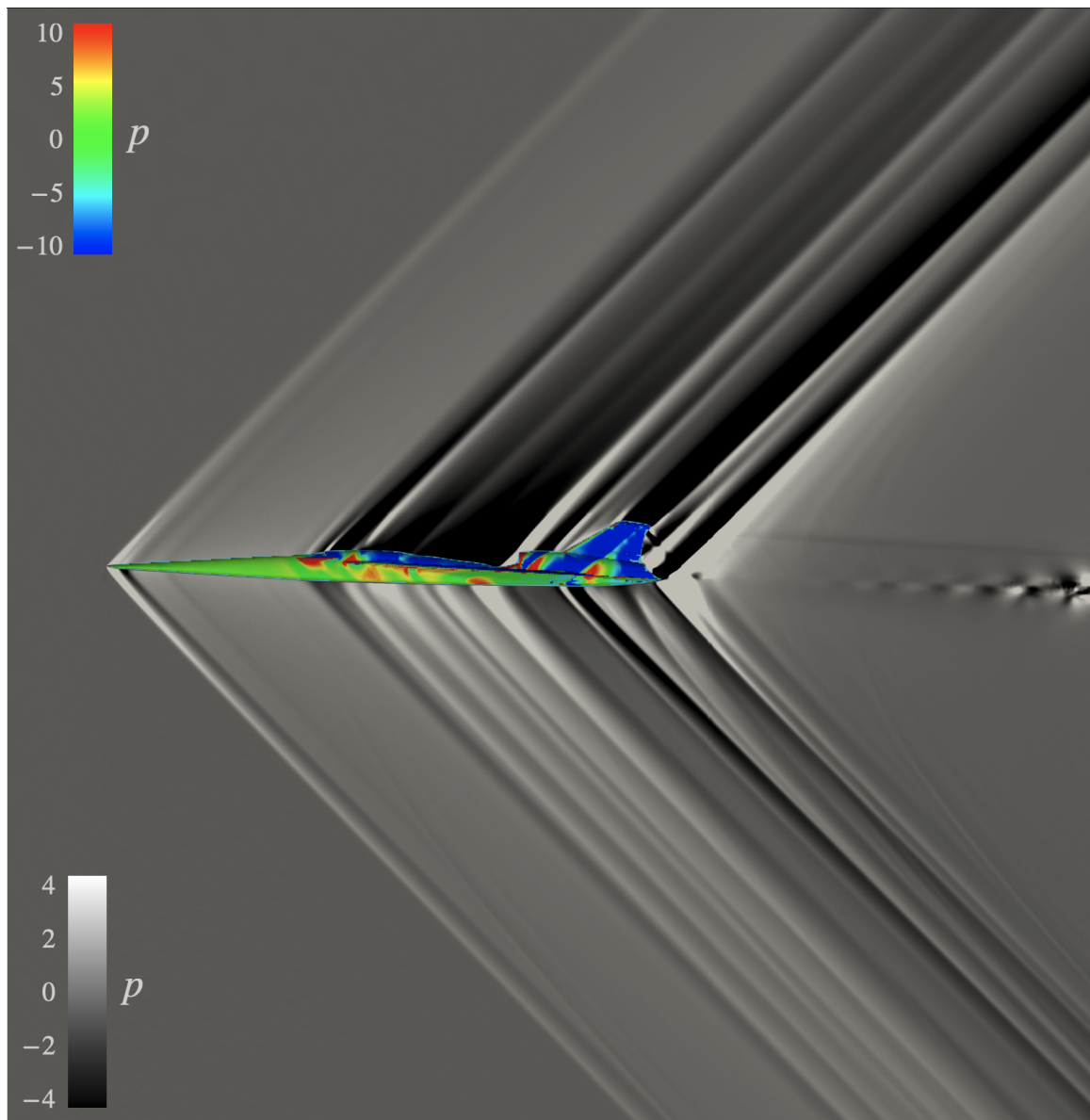


Figure 4-9: Pressure distribution from  $x$ - $z$  plane.

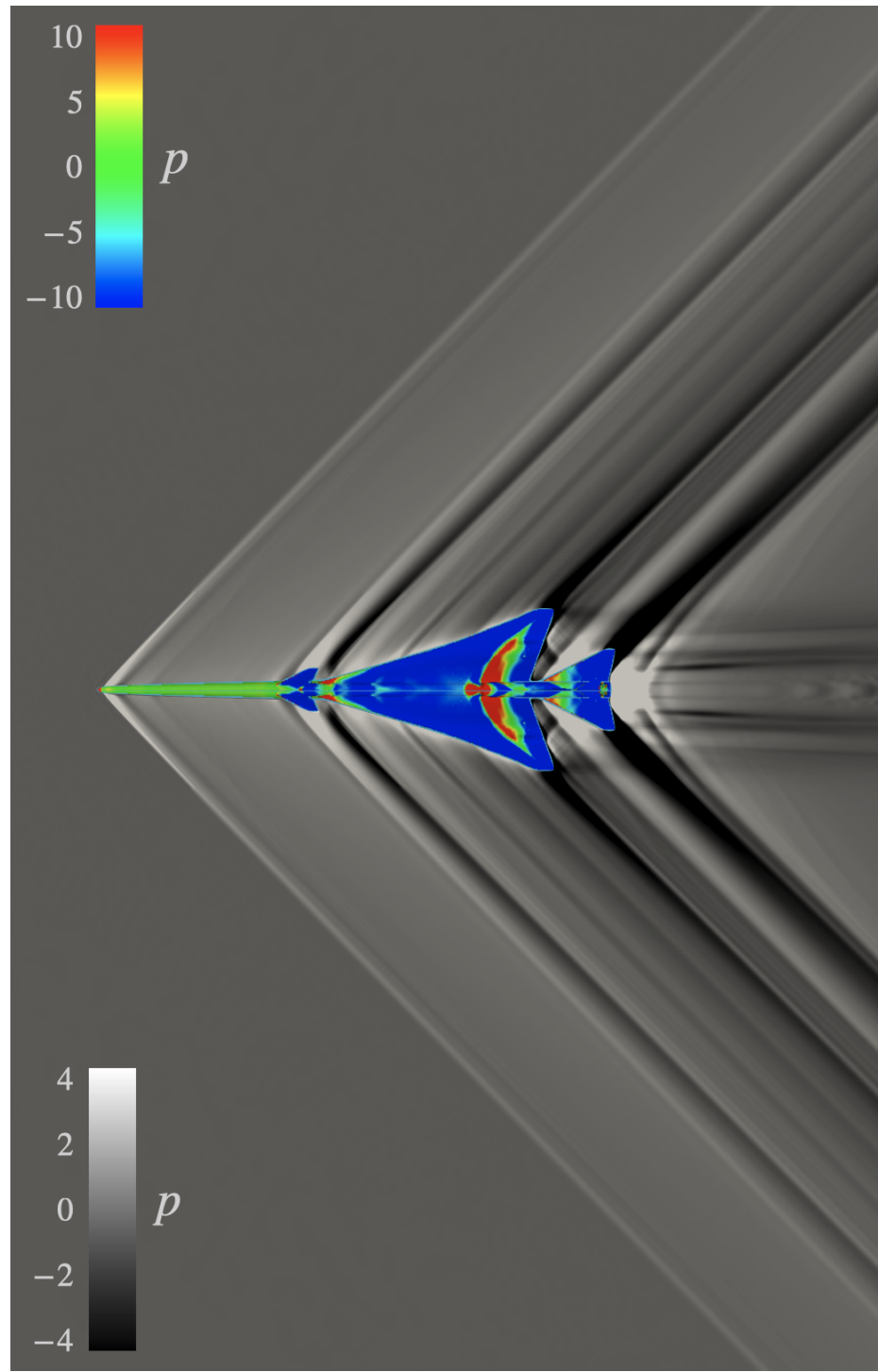


Figure 4-10: Pressure distribution from  $x$ - $y$  plane.

### 4.3.2 Pressure signatures

We assess the prediction of the near-field pressure signature from WMLES. We define a transformed x-coordinate given by

$$X_N = x - \frac{L_{BODY}}{\tan(\mu)}, \quad (4.3)$$

where the distance from the nose in the freestream direction  $x$  is normalized by the Mach angle  $\mu = \sin^{-1}(1/M)$  using the radial distance to the model,  $L_{BODY}$  in this case. This transformation is common for sonic boom simulations [24].

Figure 4-11 shows the prediction of the pressure signature by WMLES with the DSM SGS model for the different grid refinement configurations outlined in Table 4.3. The  $x$ -axis is  $X_N$  normalized by the length of the body  $L_{BODY}$ . The  $y$ -axis is  $p$  defined above. As the grid is refined, the prediction provided by WMLES approaches the RANS results for the near-field pressure signature. Results computed using the Vreman SGS model were comparable, and so Figure 4-12 shows the finest resolution case comparison with both SGS models.

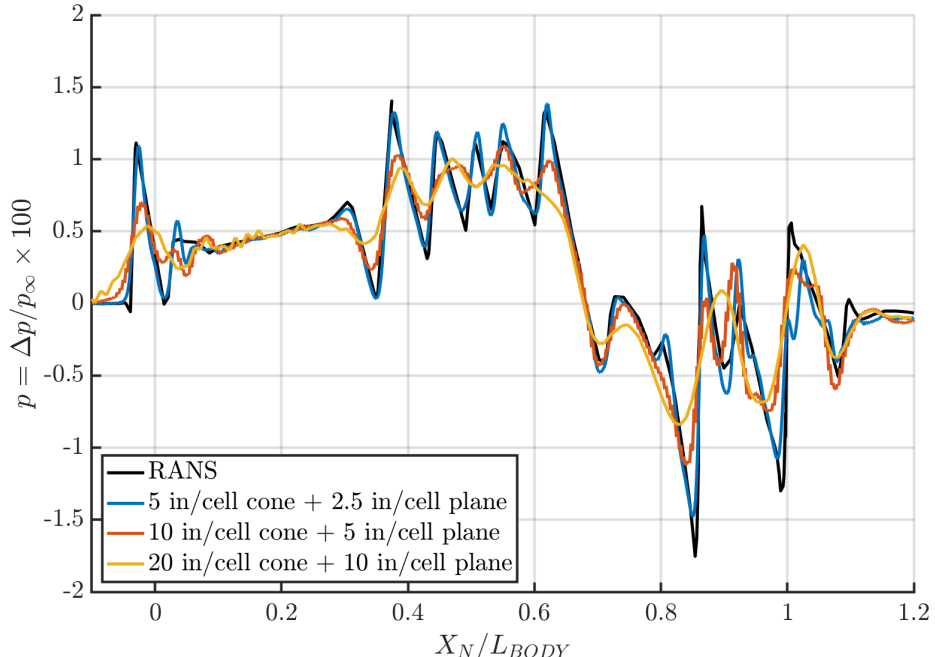


Figure 4-11: Near-field pressure signatures using DSM SGS model for different grid resolutions (cases 1-3).

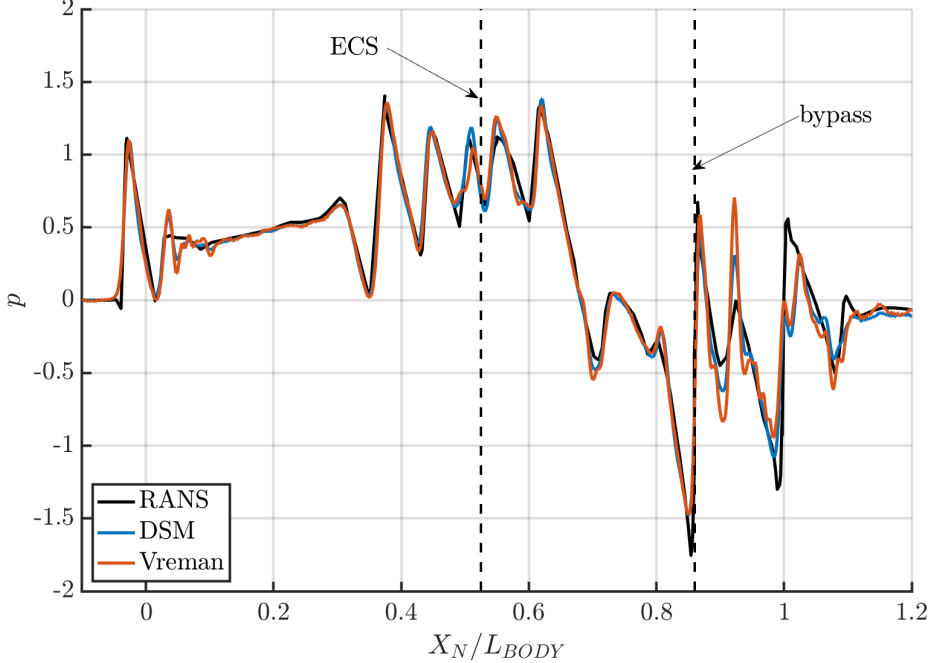


Figure 4-12: Near-field pressure signatures using Vreman and DSM SGS models (cases 3 and 6).

We see that both models for WMLES do not match the RANS solution as well further downstream and after the aircraft. Note that the additional propulsion boundary conditions at the ECS and bypass at around  $X_N/L_{BODY} \approx 0.45$  and  $X_N/L_{BODY} \approx 0.85$ , respectively, match the RANS solution with reasonable accuracy. Thus, the mismatch downstream after around  $X_N/L_{BODY} \approx 0.9$  could be due to the extremely complex interactions and rapid series of shocks and expansions near the wing trailing edge, horizontal stabilator, aft deck, T-tail, engine plume, and tip vortices [40]. Because the WMLES and RANS approximations show strong agreement before around  $X_N/L_{BODY} \approx 0.9$ , there is thought to be a deficiency in one (or both) of the approximations following the separation and complex interactions in the flow following the wing trailing edge.

#### 4.3.3 Error convergence

We show the results for convergence in the pressure value as we refine the grid resolution in Figure 4-14. Dashed lines represent the RANS solution for reference and

are not dependent the grid resolution along the  $x$ -axis. The  $X_N/L_{BODY}$  locations of interest are shown in the schematic in Figure 4-13 for reference to give insight into which areas of the geometry are impactful at the location of the pressure probe. We see that the pressure value approaches the RANS data as the grid is refined. Further, we see that the WMLES approximation of the pressure value is very comparable to the RANS data for the most refined grid configuration.

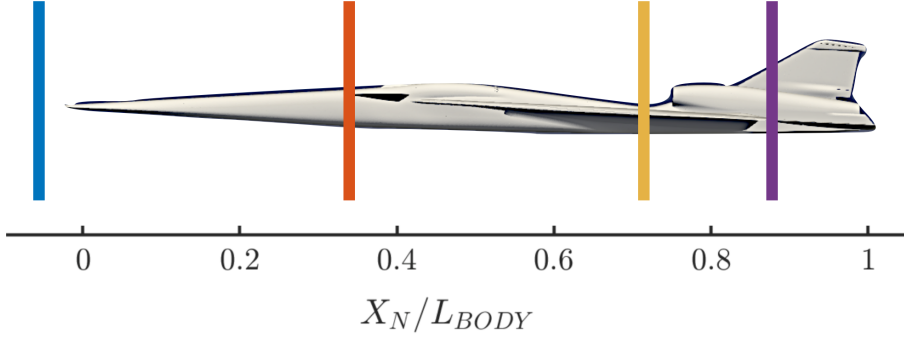


Figure 4-13: Schematic of aircraft with delineations at specified locations.

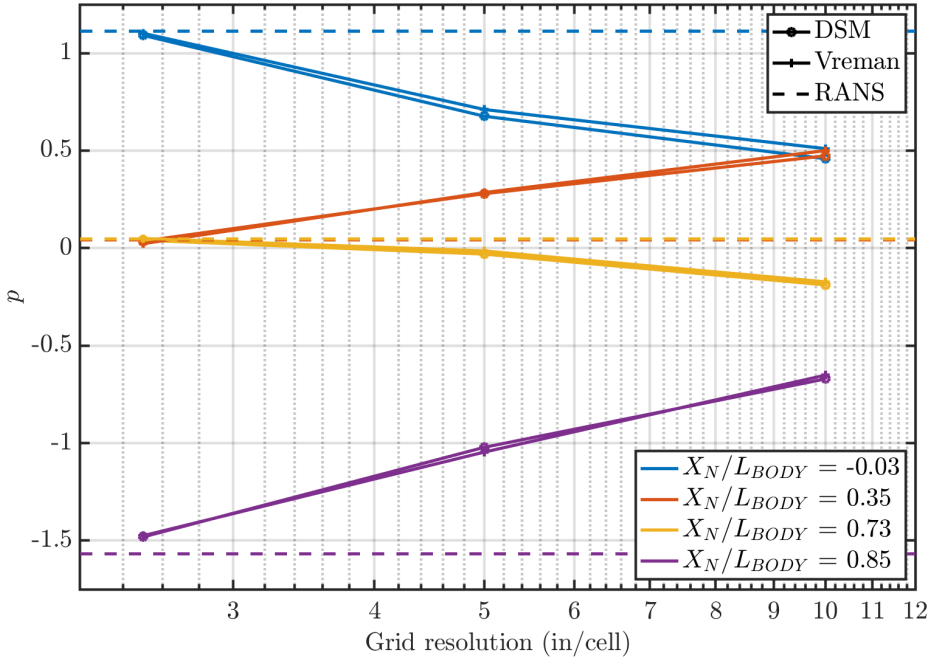


Figure 4-14: Pressure convergence for different grid resolutions.

We can also perform a similar error analysis as in the previous chapter, this time assuming that RANS provides the “true” value. We define the error in the pressure

signature prediction as

$$\varepsilon_p = \frac{p_{\text{LES}} - p_{\text{RANS}}}{p_{\text{RANS}}}, \quad (4.4)$$

where the subscripts denote either the LES or RANS solution. We also show these results for convergence in the error in the error in Figure 4-15.

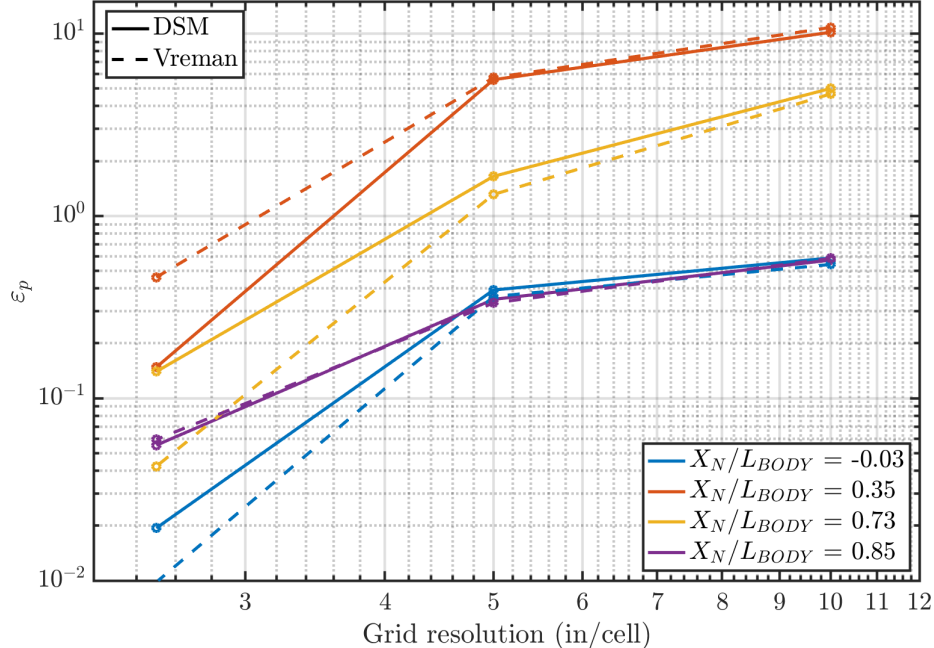


Figure 4-15: Error convergence for near-field pressure signature prediction.

To quantify the overall accuracy of the predictions provided by WMLES with the different SGS models used, we can calculate the average difference between the pressure quantity of interest  $p$  (which is already in units of percent) across all of the interpolated probe locations normalized by the number of probes defined by

$$\langle \varepsilon_p \rangle = \sqrt{\frac{1}{n} \sum_{i=1}^n (p_{\text{LES}_i} - p_{\text{RANS}_i})^2}, \quad (4.5)$$

where  $i$  is an interpolated probe point, and  $n$  is the total number of points in the pressure probe. The expression represents the  $L_2$  norm divided by the square root of the number of probe points.

The results are tabulated in Table 4.4. We include the  $L_2$  norm for each grid

resolution configuration for both models used. We interpolate the RANS solution onto the LES probe locations for each case before calculating the  $L_2$  norm. We see that the average difference gets smaller as the grid is refined, which means that the prediction by WMLES matches better with the RANS results, supporting our conclusions.

Table 4.4:  $L_2$  norms for near-field pressure signature predictions

	DSM	Vreman
20 in/cell cone + 10 in/cell plane	0.2522	0.2617
10 in/cell cone + 5 in/cell plane	0.2061	0.2141
5 in/cell cone + 2.5 in/cell plane	0.1198	0.1446

## 4.4 Computational cost

Cost-efficiency is part of the motivation for using WMLES for turbulence modeling. Spurlock et al. (2022) [56] performed RANS for the AIAA Sonic Boom Prediction Workshop on the X-59 on the NASA Ames Electra cluster using 1 Skylake node with two Intel Xeon Gold 6148 processors and a total of 40 cores for each run. The total computational time was 1431 CPU-hr for the finest provided adapted grid with 29.6M cells [56]. Table 4.5 outlines the calculations for the computational cost for different grid refinement configurations for the WMLES cases with the Vreman SGS model. We can compare the computational cost in CPU-hr for WMLES with the RANS value for a comparable grid size in millions of control volumes (CV). This estimate is based on 5 flow passes through the domain to ensure convergence in the solution of the pressure signature propagated to one-body length below the aircraft. The number of characteristic steps in the simulation is determined using  $\Delta t$  estimated from the Courant number. The computational time in core-s is then converted to CPU-hr. We also revisit relevant system specifications for the MIT Supercloud in Table 2.1 specific to each simulation.

Table 4.5: Computational cost estimates for WMLES with Vreman SGS model

	20 in/cell cone + 10 in/cell plane	10 in/cell cone + 5 in/cell plane	5 in/cell cone + 2.5 in/cell plane
CV (M)	3	18	135
$\Delta t$ (s)	0.15	0.075	0.0375
Characteristic steps	25,000	50,000	100,000
Normalized time (core-s/CV/step)	12		
Total nodes	5		10
Total cores	240		480
<b>CPU-hr</b>	250	3000	45,000

These estimates show that WMLES is more costly than RANS for a comparable grid resolution. For example, the 10 in/cell cone with 5 in/cell plane grid configuration has 18M control volumes, comparable to the RANS simulation with 29.6M control volumes. The total computational time for WMLES for this particular solver is estimated to be about 3000 CPU-hr. We would expect to see improvements in the computational cost by optimizing the solver, using faster CPUs, or using GPUs to get 7 to 10 times faster turnaround. We plot the relationship between the number of control volumes in the mesh to the total computational cost in CPU-hr in Figure 4-16. We see that the cost increases at a rate faster than the power law of the number of control volumes. For the finest WMLES grid size, the pressure signature adequately matches the RANS solution. So, these cost estimates motivate future work in developing better models that are more accurate for relatively coarser grids, which would directly result in a decreased computational cost and faster convergence of the solution computed by WMLES.

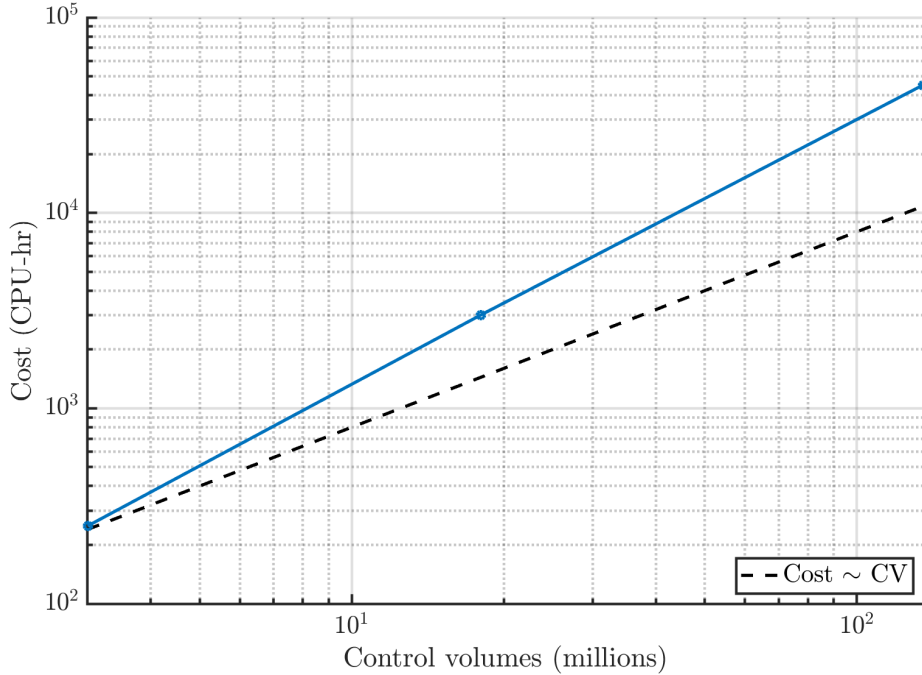


Figure 4-16: Computational cost for number of control volumes in millions.

## 4.5 Conclusions

From these results, we see that WMLES is able to predict the near-field pressure signature with very reasonable accuracy compared to RANS results. We see less accuracy for WMLES for both models downstream from the aircraft. This could be due to the extremely complex interactions near and around the tail. Additionally, for a comparable grid resolution, WMLES is not able to capture the peaks as well as RANS in both the magnitude of the pressure and the location of the shock. Further, based on findings from the previous chapter, we would expect the errors in predicting statistical quantities of interest to increase as Mach number increases, even for very refined grids. Thus, we want to look toward improvements in the SGS models to result in better predictions even with coarser grids that are more computationally affordable to generate and calculate the flow field solution. Further, the assessment of the computational cost prompts continued interest toward WMLES modeling improvements to be able to generate more accurate predictions for coarser and cheaper grids.

It is important to assess the validity of assuming that RANS is the “truth” when making comparisons. RANS-based turbulence modeling is the industry standard for aerospace applications due to usability and computational efficiency. While these solvers are generally able to capture wall-bounded flows, RANS is often unable to accurately and reliably predict turbulent flows with significant regions of separation [53, 23, 1]. For high-speed applications with complex geometries, such as the X-59, we see just that. It is known that the accuracy of RANS results often falls after massive separation in a turbulent flow [55]. It has also been shown that RANS is not as accurate for unsteady flows in high-lift applications [11, 35]. Because RANS simulations capture the flow field up to large scales of turbulent structures, it could be possible that areas dependent on the grid resolution do not capture these structures well, leading to inaccuracies that propagate [35]. Thus, it is important to consider the accuracy of the reference data when assessing the prediction from WMLES. Regardless, future work for increasing the fidelity of WMLES includes developing more accurate SGS models, as we demonstrated in the previous chapter for channel flow.

# Chapter 5

## Conclusions

### 5.1 Summary

In this thesis, we studied two different high-speed applications: a canonical channel flow and an external aerodynamic application, the Lockheed Martin X-59 QueSST aircraft. The intention was to address outstanding limitations of WMLES in predicting certain quantities of interest when compressibility effects are considered.

Error scaling properties for the compressible canonical channel flow at high speeds at different flow conditions and grid resolutions were quantified. Quantities of interest included the mean temperature profile, mean velocity profile, heat flux at the wall, and skin friction coefficient. It was found that errors in predicting mean quantities of interest were lowest overall with error in predicting the mean velocity profile less than 1% and error in predicting the mean temperature profile around 10%. Wall quantities showed the highest errors with error in predicting the heat flux at the wall approaching 70% and error in predicting the skin friction coefficient around 30%. The errors scaled with Mach number for all quantities considered, demonstrating the importance of compressibility effects. We also saw dependence on the grid resolution in some cases. Lastly, dependence on the Reynolds number became less significant for higher speed flows.

Further, we applied a new SGS model based on information theory to the high-speed channel flow and assessed improvements in predicting the mean quantities of

interest. The model aims at minimizing the information lost between the probability mass distribution of the interscale energy transfer and viscous dissipation at different scales. We saw comparably accurate prediction of the mean velocity profile within 1% of DNS data. The IP SGS model outperformed the traditional DSM SGS model in predicting the mean temperature profile, with 5% improvement when compared to DNS results. This demonstrated the potential of an information-theoretic formulation to be an effective framework for reduced-order modeling for fluid dynamics.

Lastly, we performed a novel WMLES of a full-sized external aerodynamic application, the X-59 QueSST, at cruise conditions of  $M = 1.4$  and  $Re/in = 109,776$ . The performance of traditional SGS models in predicting the near-field pressure signatures and the intensities and locations of the shock waves was assessed. Error and convergence properties were assessed in comparison to RANS results provided by the AIAA Sonic Boom Prediction Workshop. The intensities and locations of the shock waves were well-captured by WMLES and agreed with previous numerical studies from RANS. It was found that the WMLES prediction of the near-field pressure signature matched the RANS results within 3% when using a very refined grid. We saw similar predictions for both DSM and Vreman SGS models. WMLES is shown to be more computationally expensive than the same simulation performed with RANS. This further motivates investment toward developing more accurate models such that WMLES predictions are comparably accurate without requiring a very refined and computationally expensive grid.

Overall, in this work, we were able to quantify errors in the WMLES prediction of quantities of interest in two high-speed applications where compressibility is important. We explored novel modeling approaches and applications for WMLES of current interest to industry and academia.

## 5.2 Outlook

There are many promising research directions that can be explored based on the results in this work. There are interesting avenues for improving the prediction of

quantities of interest in the near-field CFD domain for the X-59 and external aerodynamic applications in general. Output-driven mesh adaptation would be useful to avoid a heavily manual mesh generation process that also results in excessive refinement in unimportant areas. Wintzer et al. (2008) [68] used mesh adaptation with an embedded-boundary Cartesian meshing scheme for sonic boom simulations. The approach refines the volume mesh automatically to minimize discretization errors in pressure signatures several body-lengths away from the aircraft geometry. Further, the results show that accuracy of the propagated signal can be improved while still decreasing the total number of cells in the mesh. Park and Darmofal (2010) [41] used an adaptive method by specifying an integral of offbody pressure signature as the output for the midfield CFD domain. The cut-cell approach uses the median dual of a tetrahedral background grid is used to produce highly refined, shock-aligned anisotropic grids without prior knowledge of shock locations. Vanharen et al. (2021) [60] applied anisotropic adaptive-mesh metrics formulated to control estimated Mach interpolation error and estimated integrated near-field pressure signature error to the X-59 geometry for the AIAA Sonic Boom Prediction Workshop. A further extension could be the use of the mesh optimization via error sampling and synthesis (MOESS) mesh adaptation framework from Yano and Darmofal (2012) [69] as demonstrated in work with the MIT Solution Adaptive Numerical Simulator (SANS) code from Ursachi et al. (2021) [59], Galbraith et al. (2021) [16], and Carson et al. (2020) [5]. The algorithm for “output-based” adapted meshes produces a series of increasingly refined adapted meshes are generated using error sampling until convergence of some quantity of interest is reached [13].

Propagation of the near-field pressure signatures to resolve the loudness of the sonic boom on the surface is a natural progression of the work in this thesis. Boom propagation is modeled by solving an augmented Burgers equation that includes the effects of second-order nonlinearity, absorption, molecular relaxation, atmospheric stratification, and spreading. Rallabhandi and Loubeau (2021) [45] provided a summary for the propagation portion of the AIAA Sonic Boom Prediction Workshop. The X-59 demonstrates unique boom shaping technologies and addresses system integra-

tion challenges associated with limiting maximum sonic boom perceived level (PL) of loudness to less than 75 dB across the carpet while flying at supersonic speeds [45]. The propagation portion also should include consideration of atmospheric properties and terrain of the region. The sonic boom prediction code sBOOM by Rallabhandi (2011) [44] includes the ability to predict ground signatures in the presence of wind profiles and nonstandard atmospheres. The efficiency and accuracy of this method makes it a useful design tool in supersonic aircraft development. A recent advancement in sonic boom design has been the development of gradient-based optimization techniques utilizing an adjoint approach to efficiently determine design sensitivities from the geometry through the near-field CFD analysis and finally the propagation to the ground [9]. Darmofal et al. (2023) [10] demonstrated significant computational savings in using the output-based adaptive, higher-order finite element method for propagation of an N-wave near-field signature to the ground. For this work, it would be interesting to assess the impact of the differences in the near-field of the WMLES results compared to RANS on the sonic boom noise.

Lastly, further work in developing SGS models that can predict key statistical quantities of interest directly related to compressibility effects encountered in high-speed flow applications is ongoing. This includes SGS modeling for heat flux, skin friction coefficient, and other quantities of interest on the surface for wall-bounded flows as well as shock capturing techniques to account for discontinuities in high-speed flows generated by complex geometries. Specifically, rigorous SGS modeling for compressible flows requires consideration of additional SGS terms, such as the pressure-dilatation and the turbulent dissipation rate, that are normally neglected [62]. In simulations with high-speed boundary layers, SGS terms arising from the viscous work done by the model is sometimes neglected, resulting in an inaccurate thermal boundary condition being provided to the wall model [2]. It is expected that new SGS models will be developed that account for phenomena present in high-speed turbulent flows.

In essence, limitations of WMLES are compounded when compressible turbulent flows are introduced. Errors in the prediction of key statistical quantities of inter-

est have been quantified in this work, and reduction methods have been presented, explored, and applied for grid refinement and model improvement. Further work in these areas is expected to continue as we attempt to improve the state-of-the-art for CFD for compressible applications from canonical flows to supersonic aircraft.



# Appendix A

## Non-dimensional compressible conservation equations

We start from the governing equations for compressible flow using the temperature form of the conservation of energy

$$\frac{\partial \rho}{\partial t} + \frac{\partial \rho u_j}{\partial x_j} = 0, \quad (\text{A.1})$$

$$\frac{\partial \rho u_i}{\partial t} + \frac{\partial \rho u_i u_j}{\partial x_j} = -\frac{\partial p}{\partial x_i} + \frac{\partial \sigma_{ij}}{\partial x_j}, \quad (\text{A.2})$$

$$\frac{\partial}{\partial t}(\rho C_v T) + \frac{\partial}{\partial x_j}(\rho u_j C_v T) = -p \frac{\partial u_j}{\partial x_j} + \sigma_{ij} \frac{\partial u_i}{\partial x_j} - \frac{\partial Q_j}{\partial x_j}, \quad (\text{A.3})$$

where the variables are defined in Chapter 2. To acquire the non-dimensional forms, we employ the following reference quantities

$$t^* = t/(l/U_0), \quad x^* = x/l,$$

$$\rho^* = \rho/\rho_0, \quad u^* = u/U_0,$$

$$p^* = p/(\rho_0 U_0^2), \quad \sigma^* = \sigma/(\mu_0 U_0/l),$$

$$C_v^* = C_v/C_v^0, \quad T^* = T/T_0,$$

$$Q^* = -\kappa^* \partial T^* / \partial x^* = Q/[(\mu_0 C_p^0 / \text{Pr})(T_0/l)]$$

The continuity equation becomes

$$\frac{\partial \rho}{\partial t} + \frac{\partial \rho u_j}{\partial x_j} = 0 \quad (\text{A.4})$$

$$\frac{\rho_0 U_0}{l} \frac{\partial \rho^*}{\partial t^*} + \frac{\rho_0 U_0}{l} \frac{\partial \rho^* u_j^*}{\partial x_j^*} = 0 \quad (\text{A.5})$$

$$\frac{\partial \rho^*}{\partial t^*} + \frac{\partial \rho^* u_j^*}{\partial x_j^*} = 0 \quad (\text{A.6})$$

The momentum equation becomes

$$\frac{\partial \rho u_i}{\partial t} + \frac{\partial \rho u_i u_j}{\partial x_j} = -\frac{\partial p}{\partial x_i} + \frac{\partial \sigma_{ij}}{\partial x_j} \quad (\text{A.7})$$

$$\frac{\rho_0 U_0^2}{l} \frac{\partial \rho^* u_i^*}{\partial t^*} + \frac{\rho_0 U_0^2}{l} \frac{\partial \rho^* u_i^* u_j^*}{\partial x_j^*} = -\frac{\rho_0 U_0^2}{l} \frac{\partial p^*}{\partial x_i^*} + \frac{\mu_0 U_0}{l^2} \frac{\partial \sigma_{ij}^*}{\partial x_j^*} \quad (\text{A.8})$$

$$\frac{\partial \rho^* u_i^*}{\partial t^*} + \frac{\partial \rho^* u_i^* u_j^*}{\partial x_j^*} = -\frac{\partial p^*}{\partial x_i^*} + \frac{\mu_0}{U_0 l \rho_0} \frac{\partial \sigma_{ij}^*}{\partial x_j^*} \quad (\text{A.9})$$

$$\frac{\partial \rho^* u_i^*}{\partial t^*} + \frac{\partial \rho^* u_i^* u_j^*}{\partial x_j^*} = -\frac{\partial p^*}{\partial x_i^*} + \frac{1}{\text{Re}} \frac{\partial \sigma_{ij}^*}{\partial x_j^*} \quad (\text{A.10})$$

The temperature form of the energy equation becomes

$$\begin{aligned} \frac{\rho_0 U_0 C_v^0 T_0}{l} \frac{\partial}{\partial t^*} (\rho^* C_v^* T^*) + \frac{\rho_0 U_0 C_v^0 T_0}{l} \frac{\partial}{\partial x_j^*} (\rho^* u_j^* C_v^* T^*) = \\ -\frac{\rho_0 U_0^3}{l} p^* \frac{\partial u_j^*}{\partial x_j^*} + \frac{\mu_0 U_0^2}{l^2} \sigma_{ij}^* \frac{\partial u_i^*}{\partial x_j^*} - \frac{\mu_0 C_p^0}{\text{Pr}} \frac{T_0}{l^2} \frac{\partial Q_j^*}{\partial x_j^*} \end{aligned} \quad (\text{A.11})$$

$$\begin{aligned} C_v^0 \frac{\partial}{\partial t^*} (\rho^* C_v^* T^*) + C_v^0 \frac{\partial}{\partial x_j^*} (\rho^* u_j^* C_v^* T^*) = \\ -\frac{U_0^2}{T_0} p^* \frac{\partial u_j^*}{\partial x_j^*} + \frac{\mu_0 U_0}{\rho_0 T_0 l} \sigma_{ij}^* \frac{\partial u_i^*}{\partial x_j^*} - \frac{\mu_0 C_p^0}{\rho_0 U_0 l \text{Pr}} \frac{\partial Q_j^*}{\partial x_j^*} \end{aligned} \quad (\text{A.12})$$

$$\begin{aligned} \frac{C_v^0}{\gamma R} \frac{\partial}{\partial t^*} (\rho^* C_v^* T^*) + \frac{C_v^0}{\gamma R} \frac{\partial}{\partial x_j^*} (\rho^* u_j^* C_v^* T^*) = \\ -\frac{U_0^2}{\gamma R T_0} p^* \frac{\partial u_j^*}{\partial x_j^*} + \frac{\mu_0 U_0}{\rho_0 l \gamma R T_0} \sigma_{ij}^* \frac{\partial u_i^*}{\partial x_j^*} - \frac{\mu_0 C_p^0}{\rho_0 U_0 l \gamma R \text{Pr}} \frac{\partial Q_j^*}{\partial x_j^*} \end{aligned} \quad (\text{A.13})$$

$$\begin{aligned} \frac{C_v^0}{\gamma R} \frac{\partial}{\partial t^*} (\rho^* C_v^* T^*) + \frac{C_v^0}{\gamma R} \frac{\partial}{\partial x_j^*} (\rho^* u_j^* C_v^* T^*) = \\ - \frac{U_0^2}{\gamma R T_0} p^* \frac{\partial u_j^*}{\partial x_j^*} + \frac{\mu_0}{U_0 l \rho_0} \frac{U_0^2}{\gamma R T_0} \sigma_{ij}^* \frac{\partial u_i^*}{\partial x_j^*} - \frac{\mu_0}{U_0 l \rho_0} \frac{C_p^0}{\gamma R} \frac{1}{\text{Pr}} \frac{\partial Q_j^*}{\partial x_j^*} \end{aligned} \quad (\text{A.14})$$

$$\begin{aligned} \frac{C_v^0}{\gamma R} \frac{\partial}{\partial t^*} (\rho^* C_v^* T^*) + \frac{C_v^0}{\gamma R} \frac{\partial}{\partial x_j^*} (\rho^* u_j^* C_v^* T^*) = \\ - M^2 p^* \frac{\partial u_j^*}{\partial x_j^*} + \frac{M^2}{\text{Re}} \sigma_{ij}^* \frac{\partial u_i^*}{\partial x_j^*} - \frac{C_p^0}{\gamma R} \frac{1}{\text{RePr}} \frac{\partial Q_j^*}{\partial x_j^*} \end{aligned} \quad (\text{A.15})$$

$$\begin{aligned} \frac{1}{\gamma(\gamma-1)} \frac{\partial}{\partial t^*} (\rho^* C_v^* T^*) + \frac{1}{\gamma(\gamma-1)} \frac{\partial}{\partial x_j^*} (\rho^* u_j^* C_v^* T^*) = \\ - M^2 p^* \frac{\partial u_j^*}{\partial x_j^*} + \frac{M^2}{\text{Re}} \sigma_{ij}^* \frac{\partial u_i^*}{\partial x_j^*} - \frac{1}{\gamma-1} \frac{1}{\text{RePr}} \frac{\partial Q_j^*}{\partial x_j^*} \end{aligned} \quad (\text{A.16})$$

$$\begin{aligned} \frac{\partial}{\partial t^*} (\rho^* C_v^* T^*) + \frac{\partial}{\partial x_j^*} (\rho^* u_j^* C_v^* T^*) = \\ - \gamma M^2 (\gamma-1) p^* \frac{\partial u_j^*}{\partial x_j^*} + \frac{\gamma M^2 (\gamma-1)}{\text{Re}} \sigma_{ij}^* \frac{\partial u_i^*}{\partial x_j^*} - \frac{\gamma}{\text{RePr}} \frac{\partial Q_j^*}{\partial x_j^*} \end{aligned} \quad (\text{A.17})$$

All together, we have the non-dimensional compressible conservation equations

$$\frac{\partial \rho}{\partial t} + \frac{\partial \rho u_j}{\partial x_j} = 0 \quad (\text{A.18})$$

$$\frac{\partial \rho u_i}{\partial t} + \frac{\partial \rho u_i u_j}{\partial x_j} = - \frac{\partial p}{\partial x_i} + \frac{1}{\text{Re}} \frac{\partial \sigma_{ij}}{\partial x_j} \quad (\text{A.19})$$

$$\frac{\partial}{\partial t} (\rho C_v T) + \frac{\partial}{\partial x_j} (\rho u_j C_v T) = - \gamma M^2 (\gamma-1) p \frac{\partial u_j}{\partial x_j} + \frac{\gamma M^2 (\gamma-1)}{\text{Re}} \sigma_{ij} \frac{\partial u_i}{\partial x_j} - \frac{\gamma}{\text{RePr}} \frac{\partial Q_j}{\partial x_j} \quad (\text{A.20})$$

where the superscripts (\*) are dropped for readability.



# Bibliography

- [1] K. Bhide and S. Abdallah. High-Order Accurate Numerical Simulation of Supersonic Flow Using RANS and LES Guided by Turbulence Anisotropy. *Fluids*, 7(12), 2022.
- [2] S. T. Bose and G. I. Park. *Wall-Modeled Large-Eddy Simulation for Complex Turbulent Flows*. Annual Review of Fluid Mechanics. 2018.
- [3] P. Bradshaw and G. P. Huang. The Law of the Wall in Turbulent Flow. *Proceedings: Mathematical and Physical Sciences*, 451(1941):165–188, 1995.
- [4] G. L. Brown and A. Roshko. On density effects and large structure in turbulent mixing layers. *J. Fluid Mech.*, 64(4):775–816, 1974.
- [5] H. A. Carson, A. C. Huang, M. C. Galbraith, S. R. Allmaras, and D. L. Darmofal. Mesh Optimization via Error Sampling and Synthesis: An Update. *AIAA Scitech 2020 Forum*, 2020.
- [6] B. T. Chu and L. S. G. Kovasznay. Non-linear interactions in a viscous heat-conducting compressible gas. *J. Fluid Mech.*, 3:494–514, 1958.
- [7] D. Chung and D. I. Pullin. Large-eddy simulation and wall modelling of turbulent channel flow. *J. Fluid Mech.*, 631:281–309, 2009.
- [8] G. N. Coleman, J. Kim, and R. D. Moser. A numerical study of turbulent supersonic isothermal-wall channel flow. *J. Fluid Mech.*, 305:159–183, 1995.
- [9] D. L. Darmofal. Sonic boom propagation through adaptive finite element methods. University of Colorado Boulder, Ann and H.J. Smead Aerospace Engineering Sciences Seminar, 2022.
- [10] D. L. Darmofal, S. R. Allmaras, and M. C. Galbraith. Sonic Boom Propagation using an Output-based Adaptive, Higher-order Finite Element Method. *AIAA Scitech 2023 Forum*, 2023.
- [11] D. Drikakis, P. Tsoutsanis, and A. F. Antoniadis. Numerical Accuracy in RANS Computations of High-Lift Multi-element Airfoil and Aircraft Configurations. *53rd AIAA Aerospace Sciences Meeting*.

- [12] A. J. Favre. The Equations of Compressible Turbulent Gases. *Institute for Statistical Mechanics of Turbulence*, 1965.
- [13] K. J. Fidkowski and D. L. Darmofal. Review of Output-Based Error Estimation and Mesh Adaptation in Computational Fluid Dynamics. *AIAA Journal*, 49(4):673–694, 2011.
- [14] J. B. Freund, S. K. Lele, and P. Moin. Compressibility effects in a turbulent annular mixing layer. Part 1. Turbulence and growth rate. *J. Fluid Mech.*, 421:299 – 267, 2000.
- [15] L. Fu, M. Karp, S. T. Bose, P. Moin, and J. Urzay. Shock-induced heating and transition to turbulence in a hypersonic boundary layer. *J. Fluid Mech.*, 909:A8, 2020.
- [16] M. C. Galbraith, C. I. Ursachi, D. Chadel, S. R. Allmaras, D. L. Darmofal, R. S. Glasby, D. L. Stefanski, J. Taylor Erwin, K. R. Holst, E. A. Hereth, J. Mukhopadhyaya, and J. J. Alonso. Comparing Multi-Element Airfoil Flow Solutions Using Multiple Solvers with Output-Based Adapted Meshes. *AIAA Journal*, 60(4):2629–2643, 2022.
- [17] M. Germano, U. Piomelli, P. Moin, and W. Cabot. A dynamic subgrid-scale eddy viscosity model. *Phys. Fluids*, 3, 1991.
- [18] C. Geuzaine and J. F. Remacle. Gmsh: A 3-D finite element mesh generator with built-in pre- and post-processing facilities. *Int. J. Numer. Meth. Engng*, 79:1309–1331, 2009.
- [19] A. Hobson and B. K. Cheng. A Comparison of the Shannon and Kullback Information Measures. *J. Stat. Phys.*, 7:301–310, 1973.
- [20] P. G. Huang and P. Bradshaw. Law of the wall for turbulent flows in pressure gradients. *AIAA Journal*, 33(4):624–632, 1995.
- [21] P. S. Iyer and M. R. Malik. Analysis of the equilibrium wall model for high-speed turbulent flows. *Phys. Rev. Fluids*, 4:074604, 2019.
- [22] S. Kawai and J. Larsson. Wall-modeling in large eddy simulation: Length scales, grid resolution, and accuracy. *Phys. Fluids*, 24(1):015105, 2012.
- [23] C. C. Kiris, A. S. Ghate, J. C. Duensing, O. M. Browne, J. A. Housman, G. D. Stich, G. Kenway, L. S. Fernandes, and L. M. Machado. High-Lift Common Research Model: RANS, HRLES, and WMLES perspectives for CLmax prediction using LAVA. *AIAA 2022-1554*, 2022.
- [24] J. Kirz. DLR TAU Near-Field Simulations for the Third AIAA Sonic Boom Prediction Workshop. *J. Aircr.*, 59(3):670–682, 2022.

- [25] A. N. Kolmogorov. The local structure of turbulence in incompressible viscous fluid for very large reynolds numbers. *Dokl. Akad. Nauk SSSR*, 30:299–303, 1941.
- [26] J. Larsson and S. Kawai. Wall-modeling in large eddy simulation: length scales, grid resolution and accuracy. *Phys. Fluids*, 24, 2012.
- [27] J. Lee, M. Cho, and H. Choi. Large eddy simulations of turbulent channel and boundary layer flows at high reynolds number with mean wall shear stress boundary condition. *Phys. Fluids*, 25(11):110808, 2013.
- [28] S. K. Lele. Chapter Nine - Turbulence in compressible flows. In Paul Durbin, editor, *Advanced Approaches in Turbulence*, pages 399–481. Elsevier, 2021.
- [29] A. Leonard. Energy Cascade in Large-Eddy Simulations of Turbulent Fluid Flows. In F.N. Frenkiel and R.E. Munn, editors, *Turbulent Diffusion in Environmental Pollution*, volume 18 of *Advances in Geophysics*, pages 237–248. Elsevier, 1975.
- [30] E. N. Lorenz. Deterministic Nonperiodic flow. *J. Atmos. Sci.*, 20:130–141, 1963.
- [31] A. Lozano-Durán and G. Arranz. Information-theoretic formulation of dynamical systems: Causality, modeling, and control. *Phys. Rev. Res.*, 4:023195, 2022.
- [32] A. Lozano-Durán and H. J. Bae. Error scaling of large-eddy simulation in the outer region of wall-bounded turbulence. *J. Comput. Phys.*, 392:532–555, 2019.
- [33] T. S. Lund and E. A. Novikov. Parameterization of subgrid-scale stress by the velocity gradient tensor. *Center for Turbulence Research, Annual Research Briefs*, 1992.
- [34] M. V. Markovin. Effects of compressibility on turbulent flows. *Mécanique de la Turbulence*, pages 365–380, 1962.
- [35] A. Matiz-Chicacausa, J. Escobar, D. Velasco, N. Rojas, and C. Sedano. RANS Simulations of the High Lift Common Research Model with Open-Source Code SU2. *Numerical Simulation of the Aerodynamics of High-Lift Configurations*, pages 93–111, 2018.
- [36] T. Mauery, J. Alonso, A. Cary, V. Lee, R. Malecki, D. Mavriplis, G. Medic, J. Schaefer, and J. Slotnick. *A Guide for Aircraft Certification by Analysis*. NASA CR-20210015404. 2021.
- [37] P. Moin and K. Mahesh. *Direct numerical simulation: a tool for turbulence research*. Annual Review of Fluid Mechanics. 1998.
- [38] P. Moin, K. Squires, W. Cabot, and S. Lee. A dynamic subgrid-scale model for compressible turbulence and scalar transport. *Phys. Fluids*, 3, 1991.

- [39] G. I. Park and P. Moin. Space-time characteristics of wall-pressure and wall shear-stress fluctuations in wall-modeled large eddy simulation. *Phys. Rev. Fluids*, 1:024404, 2016.
- [40] M. A. Park and M. B. Carter. Low-Boom Demonstrator Near-Field Summary for the Third AIAA Sonic Boom Prediction Workshop. *J. Aircr.*, 59(3):563–577, 2022.
- [41] M. A. Park and D. L. Darmofal. Validation of an Output-Adaptive, Tetrahedral Cut-Cell Method for Sonic Boom Prediction. *AIAA Journal*, 48(9):1928–1945, 2010.
- [42] T. Passot and A. Pouquet. Numerical simulation of compressible homogeneous flows in the turbulent regime. *J. Fluid Mech.*, 181:441 – 466, 1987.
- [43] S. B. Pope. *Turbulent Flows*. Cambridge University Press, 2000.
- [44] S. K. Rallabhandi. Advanced Sonic Boom Prediction Using the Augmented Burgers Equation. *J. Aircr.*, 48(4):1245–1253, 2011.
- [45] S. K. Rallabhandi and A. Loubeau. Summary of Propagation Cases of the Third AIAA Sonic Boom Prediction Workshop. *AIAA Scitech 2021 Forum*, 2021.
- [46] A. Reuther, J. Kepner, C. Byun, S. Samsi, W. Arcand, D. Bestor, B. Bergeron, V. Gadepally, M. Houle, M. Hubbell, M. Jones, A. Klein, L. Milechin, J. Mullen, A. Prout, A. Rosa, C. Yee, and P. Michaleas. Interactive supercomputing on 40,000 cores for machine learning and data analysis. In *2018 IEEE High Performance Extreme Computing Conference (HPEC)*, pages 1–6. IEEE, 2018.
- [47] O. Reynolds. An experimental investigation of the circumstances which determine whether the motion of water shall be direct or sinuous, and of the law of resistance in parallel channels. *Philos. Trans. R. Soc. London Ser. A*, 174:935–982, 1883.
- [48] O. Reynolds. On the dynamical theory of incompressible viscous flows and the determination of the criterion. *Philos. Trans. R. Soc. London Ser. A*, 186:123–161, 1894.
- [49] L. F. Richardson. Weather prediction by numerical process. 1922.
- [50] P. Sagaut, N. A. Adams, and E. Garnier. Large Eddy Simulation for Compressible Flows. Springer Dordrecht, 2009.
- [51] D. Schwamborn, T. Gerhold, and R. Heinrich. The DLR TAU-Code: Recent Applications in Research and Industry. 2006.
- [52] C. E. Shannon. A Mathematical Theory of Communication. *Bell Syst. Tech. J.*, 27:379–423, 1948.

- [53] J. P. Slotnick, A. Khodadoust, J. Alonso, D. Darmofal, W. Gropp, E. Lurie, and D.J. Mavriplis. *CFD Vision 2030 Study: A Path to Revolutionary Computational Aerosciences*. NASA CR-2014-218178. 2014.
- [54] J. Smagorinsky. General Circulation Experiments with the Primitive Equations: I. The Basic Experiment. *Monthly Weather Review*, 91(3):99–164, 1963.
- [55] P. R. Spalart and V. Venkatakrishnan. On the role and challenges of CFD in the aerospace industry.
- [56] W. M. Spurlock, M. J. Aftosmis, and M. Nemec. Cartesian Mesh Simulations for the Third AIAA Sonic Boom Prediction Workshop. *J. Aircr.*, 59(3):708–724, 2022.
- [57] A. A. Townsend. *The Structure of Turbulent Shear Flow*. Cambridge (University Press), 1976.
- [58] A. Trettel and J. Larsson. Mean velocity scaling for compressible wall turbulence with heat transfer. *Phys. Fluids*, 28, 2016.
- [59] C. I. Ursachi, M. C. Galbraith, S. R. Allmaras, and D. L. Darmofal. Output-Based Adaptive Reynolds-Averaged Navier–Stokes Higher-Order Finite Element Solutions on a Multielement Airfoil. *AIAA Journal*, 59(7):2532–2545, 2021.
- [60] J. Vanharen, A. Loseille, F. Alauzet, and M. A. Park. Nearfield Anisotropic Mesh Adaptation for the Third AIAA Sonic Boom Workshop. *AIAA Scitech 2021 Forum*, 2021.
- [61] A. W. Vreman. An eddy-viscosity subgrid-scale model for turbulent shear flow: Algebraic theory and applications. *Phys. Fluids*, 16(10):3670–3681, 2004.
- [62] B. Vreman, B. Geurts, and H. Kuerten. Subgrid-modelling in LES of compressible flow. *Appl. Sci. Res.*, 54:191–203, 1995.
- [63] Y. Wada and M. S Liou. An Accurate and Robust Flux Splitting Scheme for Shock and Contact Discontinuities. *SIAM Journal on Scientific Computing*, 18(3):633–657, 1997.
- [64] T. Weissman, E. Ordentlich, G. Seroussi, S. Verdu, and M. Weinberger. Inequalities for the  $L_1$  Deviation of the Empirical Distribution. *Hewlett-Packard Labs, Tech. Rep*, 1973.
- [65] E. Williams, G. Arranz, and A. Lozano-Durán. Wall-modeled large-eddy simulation of the lockheed martin x-59 quesst. Bulletin of the American Physical Society, 2022.
- [66] E. Williams and A. Lozano-Durán. Error scaling of wall-modeled large-eddy simulation of compressible wall turbulence. Bulletin of the American Physical Society, 2021.

- [67] E. Williams and A. Lozano-Durán. Information-Theoretic Approach for Subgrid-Scale Modeling for High-Speed Compressible Wall Turbulence. *AIAA AVIATION 2022 Forum*, 2022.
- [68] M. Wintzer, M. Namec, and M. J. Aftosmis. Adjoint-Based Adaptive Mesh Refinement for Sonic Boom Prediction. *26th AIAA Applied Aerodynamics Conference*, 2008.
- [69] M. Yano and D. L. Darmofal. An optimization-based framework for anisotropic simplex mesh adaptation. *J. Comput. Phys.*, 231(22):7626–7649, 2012.
- [70] J. Yao and F. Hussain. Turbulence statistics and coherent structures in compressible channel flow. *Phys. Rev. Fluids*, 5:084603, 2020.